

Dynamical Models of the Milky Way in Action Space with LAMOST DR8 and GAIA EDR3

GUANG-CHEN SUN,^{1,2,3} QIAO WANG,^{2,3} SHUDE MAO,⁴ YICHAO LI,¹ RICHARD J. LONG,⁴ PING-JIE DING,⁵ YOUNGANG WANG,^{2,6,3,1}
XIN ZHANG,^{1,7,8} AND XUELEI CHEN^{2,6,3,1}

¹Key Laboratory of Cosmology and Astrophysics (Liaoning)
& College of Sciences, Northeastern University, Shenyang 110819, China

²National Astronomical Observatories, Chinese Academy of Sciences, Beijing 100101, China

³School of Astronomy and Space Science, University of Chinese Academy of Sciences, Beijing 100049, China

⁴Department of Astronomy, Tsinghua University, Beijing 100084, China

⁵Purple Mountain Observatory, Chinese Academy of Sciences, Nanjing 210023, People's Republic of China

⁶Key Laboratory of Radio Astronomy and Technology, Chinese Academy of Sciences, A20 Datun Road, Chaoyang District, Beijing 100101, China

⁷National Frontiers Science Center for Industrial Intelligence and Systems Optimization, Northeastern University, shenyang 110819, China

⁸Key Laboratory of Data Analytics and Optimization for Smart Industry (Ministry of Education), Northeastern University, Shenyang 110819, China

ABSTRACT

This work explores dynamical models of the Milky Way (MW) by analyzing a sample of 86,109 K giant stars selected through cross-matching the LAMOST DR8 and Gaia EDR3 surveys. Our earlier torus models in Wang et al. (2017) did not include Gaia data, making them incompatible with the new sample's proper motion distributions. Here, we refine the construction of action-based, self-consistent models to constrain the three-dimensional velocity distribution of K giants over a larger parameter space, drawing on a series of existing MW models. This approach produces several new MW models. Our best-fit model for the local kinematics near the Sun indicates a MW virial mass of $1.35 \times 10^{12} M_{\odot}$, a local stellar density of $0.0696 M_{\odot} \text{pc}^{-3}$, and a local dark matter density of $0.0115 M_{\odot} \text{pc}^{-3}$. Our main conclusion supports a thicker and more extended thick disk, alongside a cooler thin disk, compared to the best-fitting model in Wang et al. (2017). Near the Sun, our model aligns well with observations, but is less satisfactory at distances far from the Galactic center, perhaps implying unidentified structures. Further high-precision observations will be critical for understanding the dynamics in these outer Galactic regions, and will require a more realistic model.

Keywords: Galaxy dynamics (591) — Milky Way Galaxy (1054) — Milky Way mass (1058)— Galaxy kinematics (602) — Milky Way Galaxy physics (1056) — Galaxy physics (612)

1. INTRODUCTION

To unravel the mysteries of the Milky Way (MW), astrophysicists have long sought to develop dynamical models that accurately reflect its structure and formation. The advent of high-precision observing campaigns, especially the Gaia

mission, has precipitated an unprecedented influx of data, characterizing over a billion stars with previously unmatched astrometric and photometric precision (Gaia Collaboration et al. 2016, 2018, 2021). Combining observations from large spectroscopic surveys, such as the Large Area Multi-Object Spectroscopic Telescope (LAMOST) Experiment for Galactic Understanding and Exploration (Deng et al. 2012), a large number of stars with six-dimensional phase space information has become available. It provides a unique opportunity to refine our understanding of the MW's fundamental properties, including its mass distribution, kinematic behaviors, and the elusive dark matter halo surrounding it.

Many techniques have been proposed to model the dynamics of the MW. The first technique is the Jeans method,

Corresponding author: Yougang Wang
wangyg@bao.ac.cn

Corresponding author: Xin Zhang
zhangxin@mail.neu.edu.cn

Corresponding author: Xuelei Chen
xuelei@cosmology.bao.ac.cn

based on moments of the Jeans equation and the adopted density and kinematics (Jeans 1915). Most mass measurements of the MW are obtained from the Jeans equation (e.g. Xue et al. 2008; Kafle et al. 2014; Bird et al. 2022a; Sun et al. 2023). The second method is Schwarzschild’s orbit-superposition technique (Schwarzschild 1979, 1993), which builds a steady-state model by calculating orbits in a fixed gravitational potential and determining the orbit weights required to fit the observational constraints. Using this method, a three-dimensional steady-state stellar dynamical model of the Galactic bar has been constructed (Zhao 1996), and two relatively new Galactic bar models were constructed by Wang et al. (2012, 2013). The third method is the made-to-measure (M2M) method, first proposed by Syer & Tremaine (1996). This method is close to Schwarzschild’s orbit-superposition technique, the only difference being how the Schwarzschild orbit and M2M particle weights are obtained. M2M techniques have also been used to construct the Galactic bar (Long et al. 2013; Hunt & Kawata 2013; Zhu et al. 2014; Portail et al. 2017; Webb et al. 2023).

McGill & Binney (1990) proposed a numerical method to construct action-angle tori in general gravitational potentials, and a series of following studies (Binney & Kumar 1993; Kaasalainen & Binney 1994; Valluri & Merritt 1999; McMillan & Binney 2008) described tori construction and their application to galactic dynamics. An orbital torus is associated with specific values of the actions \mathbf{J} . Once a torus has been so specified, the star’s position and velocity is determined, and the contribution to the local density from any value of the star’s angle variables θ can be obtained (Binney & McMillan 2016). This torus and action-based distribution function method is useful and powerful for modeling the dynamics of galaxies (Sanders & Binney 2016), and has distinct advantages (Binney & McMillan 2016). Recently, new self-consistent models of the MW have been introduced by the application of action-based distribution functions (DFs) (Binney & Vasiliev 2023, 2024). Meanwhile, Robin et al. (2022) used the Stäckel approximation to build a self-consistent dynamical model of the MW disk, **defining a DF in terms of three integrals of motion, energy E , angular momentum L_z , and a third integral I_3 which is assumed to be close to the truly conserved integral in the the Stäckel potential**. These studies underscore the efficacy of action-based DF methods for Galactic modeling. By leveraging integrals of motion and iteratively refining the gravitational potential, researchers can build models that remain dynamically self-consistent while aligning closely with observational constraints.

We have constructed torus models of the MW in a large volume by using the K giant stars selected from the LAMOST DR 2 catalogue (Wang et al. 2017). We found that the outer disk is much thicker than previously thought, or alter-

natively that the outer structure is not a conventional disk at all. Here we return to this topic for three main reasons. First, the sample of K giants has significantly increased; second, proper motion constraints were not used in Wang et al. (2017); and, third, dynamical modeling in action space has also been improved which enables us to construct self-consistent models in action space.

The structure of this paper is as follows. Section 2 describes the data samples used. In Section 3, we detail our models and methods. In Section 4, we present the dynamical models of the Milky Way. Section 5 summarizes our main results.

2. DATA SAMPLE

In this study, we focus on K-type giant stars, which are highly luminous and have long lifespans, making them excellent tracers for Galactic observations. Our primary dataset comes from the catalog by Ding et al. (2021), where K-type giants are identified following the criteria of Liu et al. (2014), which is based on the effective temperature (T_{eff}) and the surface gravity ($\log g$), $4000 \text{ K} < T_{\text{eff}} < 4600 \text{ K}$ with $\log g < 3.5$ and $4600 \text{ K} < T_{\text{eff}} < 5600 \text{ K}$ with $\log g < 4$. The spectroscopic data from the LAMOST eighth data release (LAMOST DR8). This identification is complemented by Gaia EDR3 proper motions and parallaxes, ensuring high accuracy. The line-of-sight velocity (v_{LOS}) measurements are taken directly from LAMOST DR8.

Neither LAMOST nor Gaia datasets are immune to systematic errors, which must be carefully addressed in the analysis (Anguiano et al. 2018; Lindegren et al. 2021). We correct the LAMOST v_{LOS} measurements by 5.7 km s^{-1} , following Tian et al. (2015) to account for observed systematic offsets. Recently, Lindegren et al. (2021) introduced a method to correct the Gaia EDR3 parallax zero-point, considering source magnitude, color, and sky position. This approach is crucial for improving distance estimates and enhancing spatial analyses. Using the corrected parallax ϖ , we derive the inverse parallax distance $D_\varpi = 1/\varpi$. Additionally, we follow Ding et al. (2021), which employed a method developed by Carlin et al. (2015) to estimate photometric distances (D_{Carlin}) using the LAMOST spectra. This dual approach to distance estimation provides a robust assessment of the spatial distribution of K giants. Section 2.1 further discusses the optimization of these distances for specific regions of interest.

To ensure high-quality data, we adhere to the following standards: for LAMOST DR8 data, we apply $S/N > 5$; for Gaia EDR3 data, we apply $\text{ASTROMETRIC_GOF_AL} \leq 3.0$, $\text{ASTROMETRIC_EXCESS_NOISE_SIG} \leq 2.0$, and a renormalized unit weight error ($RUWE$) ≤ 1.4 , selecting stars with reliable spectra and astrometry. Here, S/N represents the signal-to-noise ratio in the G-band. We compile a com-

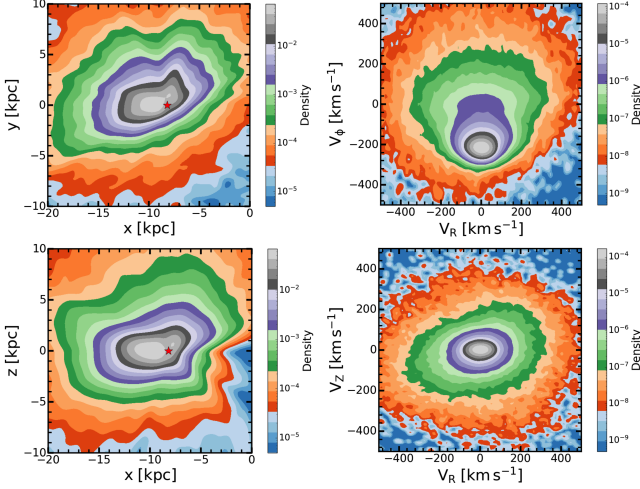


Figure 1. The projected distribution in the x-y plane (upper left), x-z plane (lower left), V_R - V_ϕ plane (upper right), and V_R - V_z plane (lower right) for all 607,833 K giants in our sample. The red stars in the left panels indicate the position of the Sun. The color mapping represents the observed density of K giants, calculated using the kernel-density estimation method with Gaussian kernels. It is important to note that this method may smooth out some fine details.

prehensive six-dimensional phase space dataset of 607,833 K giants, which forms the basis for all subsequent analyses unless otherwise stated.

We use the *Astropy* library (Astropy Collaboration et al. 2013, 2018) to transform $(\alpha, \delta, D_{\text{Carlin}}, v_{\text{LOS}}, \mu_\alpha, \mu_\delta)$ into a Cartesian coordinate system (x, y, z, v_x, v_y, v_z) centered on the Galactic center. In this system, α and δ are right ascension (R.A.) and declination, respectively, x points from the Sun towards the Galactic center, y aligned with Galactic rotation, and z directs towards the Northern Galactic Pole. Velocities v_x , v_y , and v_z are measured in the Galactic rest frame. μ_α and μ_δ correspond to α and δ . Figure 1 shows the spatial distribution of all 607,833 K giants.

The parameters required for coordinate transformation include the distance from the Sun to the Galactic center, which we set to $R_\odot = 8.178 \pm 0.035$ kpc (Gravity Collaboration et al. 2019), and the Sun’s height above the Galactic plane is set to $z_\odot = 20.8 \pm 0.3$ pc (Bennett & Bovy 2019). The motion of the Sun in the Galactic frame is represented as $v_\odot = (U_\odot, V_\odot, W_\odot) = (11.10 \pm 1.75, 12.24 \pm 2.47, 7.25 \pm 0.87)$ km s⁻¹ (Schönrich et al. 2010), where U_\odot , V_\odot , and W_\odot represent the components toward the Galactic center, in the direction of Galactic rotation, and towards the Galactic north pole, respectively. The initial potential model, hereafter Mc17 (McMillan 2017), represents the MW as an axisymmetric system comprising a bulge, thin and thick stellar disks, two gas disks, and a spherical dark matter halo. In Mc17, the circular velocity at the Sun’s position is $v_0 = 232.8 \pm 3.0$ km s⁻¹.

2.1. Suitable distance

Distances for K-type giant stars can be estimated using two methods: the inverse parallax distance from Gaia EDR3 (D_ϖ), and the photometric distance (D_{Carlin}) obtained from absolute magnitudes and stellar parameters based on LAMOST spectra (Carlin et al. 2015). While D_ϖ benefits from Gaia’s high-precision astrometric measurements (particularly for stars located nearer to the Sun), its reliability decreases for more distant objects or those with lower astrometric accuracy (Astraatmadja & Bailer-Jones 2016; Luri et al. 2018). In contrast, D_{Carlin} is less affected by these observational constraints but is more sensitive to uncertainties arising from extinction and stellar atmosphere modeling.

As noted by Ding et al. (2021), there is a close agreement between D_ϖ and D_{Carlin} , although D_ϖ tends to yield slightly smaller values. Moreover, there is a constant scale factor between these two distances. In Figure 2, we focus on stars with small relative parallax uncertainties ($\sigma_\varpi/\varpi < 0.1$) and D_{Carlin} uncertainties ($\sigma_{D_{\text{Carlin}}}/D_{\text{Carlin}} < 0.5$). The agreement between these two distance measures is better towards the north Galactic Pole than the Galactic anticenter, possibly due to the significant influence of interstellar dust in the galactic plane on photometric estimates.

This observation motivates us to apply region-specific $D_{\text{Carlin}}/D_\varpi$ ratios to reconcile the differences. Following the method of Ding et al. (2021), we use $D = D_{\text{Carlin}}/0.86$ to denote the corrected distance in the direction of the Galactic disk region and $D = D_{\text{Carlin}}/0.97$ in the polar direction, ensuring that our distance estimates are consistent and accurately reflect data uncertainties. It is noted that the scale factor 0.86 in the Galactic disk region in this paper is slightly larger (2%) than the scale factor 0.842 in Ding et al. (2021), which is used for all samples.

2.2. Sample selection

Considering the observational limitations of LAMOST, we focus our analysis on K-type giants in the Galactic anticenter to characterize the parameters of the Galactic disk. Figure 3 extends Figure 1 from Wang et al. (2017), with the new observational sample roughly doubling the previous one overall and expanding by a factor of 4–6 in more distant regions. This enlarged dataset enhances the comparative framework provided by the reference study. Our study benefits from an expanded dataset of giants, thus enriching the comparative basis established in the reference study.

In characterizing our sample of K giants as disc-specific members, we adopt velocity-dispersion parameters from Anguiano et al. (2020); Ding et al. (2021); Vieira et al. (2022). A relaxed criterion of 3σ is adopted to reduce the inclusion of stars with excessively high velocities, thereby setting the constraints as follows: $|V_R| < 200$ km s⁻¹, $-350 < V_\phi < -100$ km s⁻¹, $|V_z| < 150$ km s⁻¹, $|V_{\text{tot}}| < 600$ km s⁻¹,

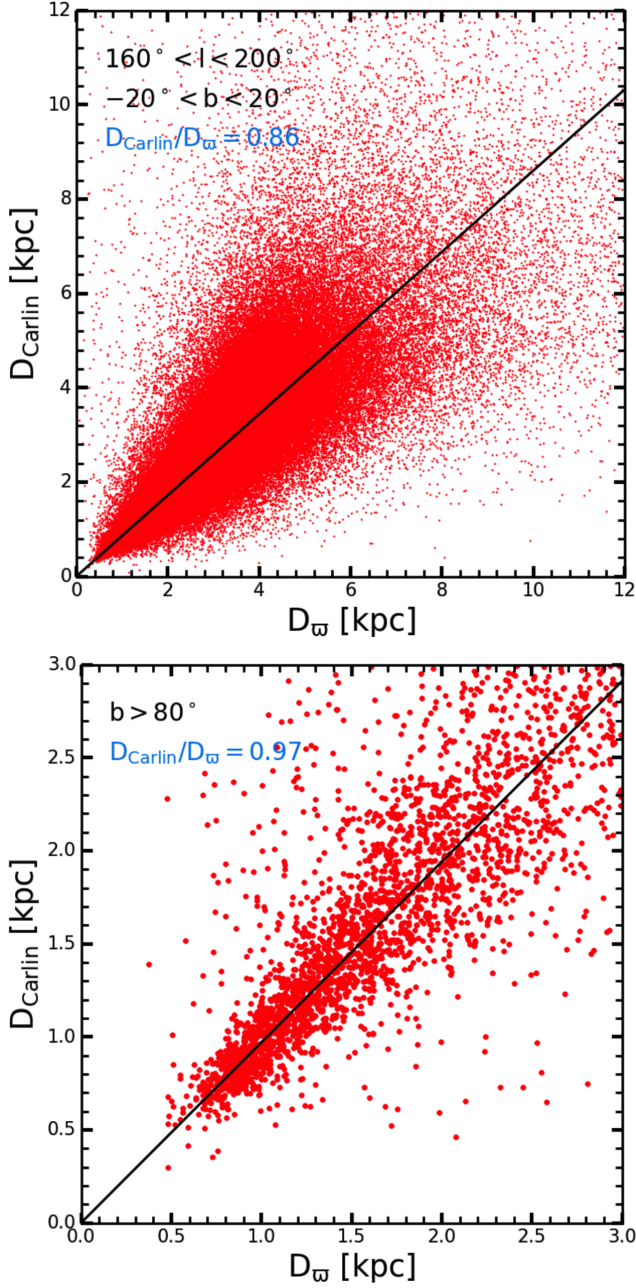


Figure 2. The comparison between photometric distance (D_{Carlin}) and parallax distance (D_{ω}) within the specified range reveals interesting trends. In the direction of the Galactic anticenter (upper panel), we observe $D_{\text{Carlin}}/D_{\omega}=0.86$, incorporating approximately 160,000 high-precision parallax measurements for K giants. Conversely, toward the north Galactic pole, this ratio is $D_{\text{Carlin}}/D_{\omega}=0.97$, based on observations of approximately 2,000 K giants.

and $[\text{Fe}/\text{H}] > -1$. Here, $V_{\text{tot}} = \sqrt{V_R^2 + V_{\phi}^2 + V_z^2}$ represents the total velocity relative to the Galactic center.

The regions of the area observed are identified in Table 1. Regions 25 and 26 are specifically allocated to encompass the

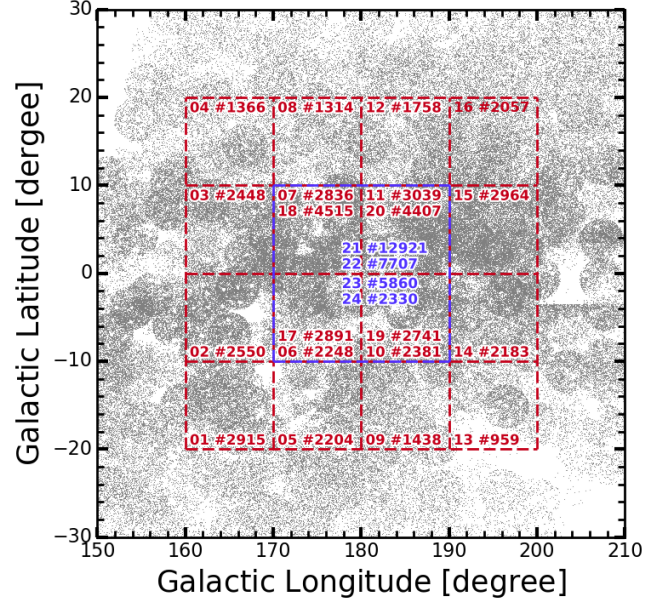


Figure 3. The selected sky regions. The figure is similar to Figure 1 in Wang et al. (2017). The labels denote the region identifier. Following the symbol ‘#’ is the number of K giants in the region. Regions 01–16 encompass giants within 2 kpc from the Sun. Regions 17, 18, 19, and 20 cover the same directions as 06, 07, 10, and 11, respectively, but extend to a depth of 2–3 kpc. Regions 21, 22, 23, and 24 cover a $20^{\circ} \times 20^{\circ}$ sky area of the Galactic anticenter from 3–12 kpc, with the blue box indicating the area covered by regions 21, 22, 23, and 24. Additionally, the grey points represent all K giants in the survey.

North Galactic Pole at a distance of up to 3 kpc to facilitate an extensive examination of the vertical kinematics. Regions 27 to 30 are strategically allocated to evaluate the validity of the potential and distribution model derived from the fitting process for the first 26 regions. These regions span four arbitrarily chosen regions close to the Galactic plane, covering distances ranging from 0 to 2 kpc.

3. METHODS

In exploring galactic dynamics, AGAMA (Action-based Galaxy Modeling Architecture) offers a sophisticated platform for developing self-consistent models of galaxies (Vasiliev 2019a). By utilizing action-angle variables, AGAMA provides a detailed and accurate method for modeling the intricate gravitational interactions that govern stellar motions and dark matter distributions, which are vital for understanding galaxy formation and evolution. For the avoidance of doubt, *self-consistent* in this context is defined as in Binney & Tremaine (2008) and is the definition used in Vasiliev (2019a). In this paper, we use AGAMA for model construction.

3.1. Action-based self-consistent methods

Table 1. The sky area is divided into regions.

	Longitude range [deg]	Latitude range [deg]	Distance [kpc]	Counts
01	(160, 170)	(-20, -10)	[0, 2]	2550
02	(160, 170)	(-10, 0)	[0, 2]	2915
03	(160, 170)	(0, 10)	[0, 2]	2448
04	(160, 170)	(10, 20)	[0, 2]	1366
05	(170, 180)	(-20, -10)	[0, 2]	2204
06	(170, 180)	(-10, 0)	[0, 2]	2248
07	(170, 180)	(0, 10)	[0, 2]	2836
08	(170, 180)	(10, 20)	[0, 2]	1314
09	(180, 190)	(-20, -10)	[0, 2]	1438
10	(180, 190)	(-10, 0)	[0, 2]	2381
11	(180, 190)	(0, 10)	[0, 2]	3039
12	(180, 190)	(10, 20)	[0, 2]	1758
13	(190, 200)	(-20, -10)	[0, 2]	959
14	(190, 200)	(-10, 0)	[0, 2]	2183
15	(190, 200)	(0, 10)	[0, 2]	2964
16	(190, 200)	(10, 20)	[0, 2]	2057
17	(170, 180)	(-10, 0)	[2, 3]	2891
18	(170, 180)	(0, 10)	[2, 3]	4515
19	(180, 190)	(-10, 0)	[2, 3]	2741
20	(180, 190)	(0, 10)	[2, 3]	4407
21	(170, 190)	(-10, 10)	[3, 4]	12921
22	(170, 190)	(-10, 10)	[4, 5]	7707
23	(170, 190)	(-10, 10)	[5, 7]	5860
24	(170, 190)	(-10, 10)	[7, 12]	2330
25	(0, 360)	(80, 90)	[0, 1.5]	1272
26	(0, 360)	(80, 90)	[1.5, 3]	1256
27	(210, 220)	(10, 20)	[0, 2]	1144
28	(140, 150)	(-10, 0)	[0, 2]	1839
29	(130, 140)	(-20, -10)	[0, 2]	1206
30	(200, 210)	(0, 10)	[0, 2]	1360

Accurately modeling galaxies presents a significant challenge due to the complex interactions among billions of stars influenced by their collective gravitational fields and dark matter. For an axisymmetric potential, there are three integrals of motion I_1, I_2, I_3 , and, by the strong Jeans Theorem, an equilibrium model can be taken as a function $f(I_1, I_2, I_3)$ of these integrals. Action integrals have several advantages over the integrals of the motion (Binney & Sanders 2014; Vasiliev 2019a) so a distribution function in AGAMA is a function of the action integrals $f(\mathbf{J})$. Density, mean velocity, the second moment of velocity, and velocity dispersion are then defined as

$$\rho(\mathbf{x}) = \iiint d^3v f(\mathbf{J}[\mathbf{x}, \mathbf{v}]), \quad (1)$$

$$\bar{\mathbf{v}} = \frac{1}{\rho} \iiint d^3v \mathbf{v} f(\mathbf{J}), \quad (2)$$

$$\overline{v_{ij}^2} = \frac{1}{\rho} \iiint d^3v v_i v_j f(\mathbf{J}) \quad (3)$$

$$\sigma_{ij}^2 = \overline{v_{ij}^2} - \bar{v}_i \bar{v}_j. \quad (4)$$

Generally, a galaxy model can be defined by specifying the DFs of each major component of stars and dark matter (Binney 2018). However, a single DF can yield different density distributions depending on the potential (Vasiliev 2018). AGAMA provides a self-consistent modelling approach, through which self-consistent density-potential pairs can be constructed. The procedure for constructing a self-consistent model has the following steps.

(i) Create a reasonable initial guess for the total density (or potential) of the whole system.

(ii) Adopt an action finder for computing the actions in the given potential.

(iii) Compute the density distribution from the DFs via Eq. 1. In practice, this step is carried out by sampling random particles in (\mathbf{x}, \mathbf{v}) space. Each (\mathbf{x}, \mathbf{v}) point is transformed into (\mathbf{J}, θ) space using the action finder.

(iv) Recalculate the potential by solving the Poisson equation with the updated density distribution.

(v) Repeat from step (ii), until the changes in potential are negligible, and the potential has converged as described in Section 5.2 of Vasiliev (2019a). Typically, five iterations are enough with a good initial guess, and 10 iterations are sufficient in practice even with a poor guess.

For computational details, the reader is referred to Vasiliev (2018). The operational steps in this work are as follows.

(1) Initial preparations: Gather observational data, calibrate distances, and divide the sky into specific regions (see Section 2).

(2) Create velocity distributions: For each sky region, bin the three velocity components ($v_{\text{LOS}}, \mu_\alpha, \mu_\delta$) of the observed K giants in International Celestial Reference System (hereafter ICRS) coordinates. The resulting histograms visualize the velocity distributions in each direction.

(3) The parameters of the relevant distribution functions are initially set using values of density and distribution function parameters from existing references as initial values. Utilize the AGAMA code to construct a self-consistent model, and use this model to produce 300 million simulated data points, each representing a K giant, to create the simulated (model) distribution histograms. **In order to increase the calculation speed, the number of iterations is set to three.**

(4) Perform least χ^2 fits. Evaluate how well the model fits the data using the Nelder–Mead optimization method to search for χ^2 minima. The DF parameters are set as free, and we use step (3) to construct the self-consistent model. The χ^2

is defined as

$$\chi^2 = \sum_n \frac{(p_n^{\text{data}} - p_n^{\text{mod}})^2}{\sigma_n^2}, \quad (5)$$

where p_n^{data} denotes the observed velocity dispersion, and σ_n the corresponding errors. p_n^{mod} represents the model prediction. The overall χ^2 used for model comparison is computed as the average of the reduced χ^2 values across all regions.

(5) After step (4), we have a series of DFs from the preliminary self-consistent models. **We now use these DFs to construct the self-consistent models again.** We iterate this process 10 times and take the final self-consistent model for each DF distribution into our analyses. All results shown in this paper are based on 10 iterations for the construction of the self-consistent model of the MW, unless stated otherwise. **The χ^2 values are obtained by generating 300 million points from the final self-consistent model and fitting the kinematics predicted by these points. The scheme of the operational steps is summarized in Figure 4.**

As shown in Figure 2, the stellar distances are not very precise, and cause some stars to move into adjacent bins, thus distorting the line-of-sight velocity and PM distributions. Based on the position and velocity of each star, we assume a normal distribution for using the observed velocity values as the means and the observational errors as the standard deviations. We then randomly generate 1,000 values for each velocity, resulting in a new sample pool that is 1,000 times larger than the original. Subsequently, we perform repeated sampling from this pool, drawing a dataset equivalent in size to the original sample each time to compute the distribution. This sampling process is repeated 1,000 times, after which the median and error of these 1,000 samples are calculated, yielding the final p_n^{data} and σ_n values.

3.2. Density and potential

The density ρ and potential Φ profiles of a galaxy model are related to each other by the Poisson's equation

$$\nabla^2 \Phi(\mathbf{x}) = 4\pi G \rho(x). \quad (6)$$

The MW model adopted in this paper is assumed to be axisymmetrical and comprises a spheroidal bulge and a spheroidal dark matter halo, two stellar disks, an HI gas disk, and a molecular gas disk.

For disk components, the density profile is modeled as (Vasiliev 2019a)

$$\rho = \Sigma_0 \exp\left(-\frac{R}{R_d} - \frac{R_{\text{cut}}}{R}\right) \times \begin{cases} \delta(z) & \text{if } h = 0, \\ \frac{1}{2h} \exp\left(-\left|\frac{z}{h}\right|\right) & \text{if } h > 0, \\ \frac{1}{4|h|} \text{sech}^2\left(\left|\frac{z}{2h}\right|\right) & \text{if } h < 0, \end{cases} \quad (7)$$

where $R = \sqrt{x^2 + y^2}$ represents the cylindrical radius, R_d is the scale radius, Σ_0 is the central surface density (value at $R = 0$), and h is the scale height. The AGAMA framework designates $h > 0$ corresponds to an exponential disk, typically applied to stellar disks, while $h < 0$ corresponds to an isothermal disk, typically applied to gas disks, with R_{cut} indicating the inner cutoff radius, adjusted according to the gas disks.

The spheroidal components, including the bulge and dark matter halo, have a density profile expressed as

$$\rho = \rho_0 \left(\frac{\tilde{r}}{r_0}\right)^{-\gamma} \left(1 + \frac{\tilde{r}}{r_0}\right)^{\gamma-\beta} \times \exp\left[-\left(\frac{\tilde{r}}{r_{\text{cut}}}\right)^2\right], \quad (8)$$

where

$$\tilde{r} = \sqrt{x^2 + y^2 + (z/q)^2} \quad (9)$$

defines the ellipsoidal radius, ρ_0 is the volume density at scale radius r_0 , and q is the axial ratio z/x of the isodensity surfaces. The parameters β and γ represent the power-law indices of the density profile in the outer and inner regions, respectively, with r_{cut} marking the outer cutoff radius.

3.3. Distribution function

In the analysis of MW dynamics, the distribution function (DF) of disk components is modeled using the quasi-isothermal framework as described in several studies (Binney 2010; Binney & McMillan 2011; Binney 2012; Piffi et al. 2014). This model assumes that the orbits are predominantly circular, thus orbits with high eccentricity and orbits that are significantly tilted to the disk plane are physically improbable (Binney & Vasiliev 2023). To prove that this model is suitable for our study, we evaluate the eccentricity of disk giants in our dataset, as shown in Figure 5. Most of these orbits exhibit low eccentricities, confirming that the quasi-isothermal model is suitable for our analysis.

The quasi-isothermal DF is mathematically expressed as

$$f(\mathbf{J}) = \frac{\tilde{\Sigma}\Omega}{2\pi^2\kappa^2} \times \frac{\kappa}{\tilde{\sigma}_r^2} \exp\left(-\frac{\kappa J_r}{\tilde{\sigma}_r^2}\right) \times \frac{\nu}{\tilde{\sigma}_z^2} \exp\left(-\frac{\mu J_z}{\tilde{\sigma}_z^2}\right) \times \begin{cases} 1 & \text{if } J_\phi > 0, \\ \exp\left(\frac{2\Omega J_\phi}{\tilde{\sigma}_r^2}\right) & \text{if } J_\phi < 0, \end{cases} \\ \tilde{\Sigma}(R_c) \equiv \Sigma_0 \exp(R_c/R_d), \\ \tilde{\sigma}_r^2(R_c) \equiv \sigma_{r0}^2 \exp(-2R_c/R_{\sigma_r}) + \sigma_{\text{min}}^2, \\ \tilde{\sigma}_z^2(R_c) \equiv \sigma_{z0}^2 \exp(-2R_c/R_{\sigma_z}) + \sigma_{\text{min}}^2, \quad (10)$$

where J_R , J_z , and J_ϕ correspond to the radial, vertical, and azimuthal components, respectively, within a cylindrical coordinate system. The azimuthal action J_ϕ is calculated as $J_\phi \equiv L_z = x \times v_y - y \times v_x$. L_z is the z -component of the angular momentum L in Cartesian coordinates. In addition,

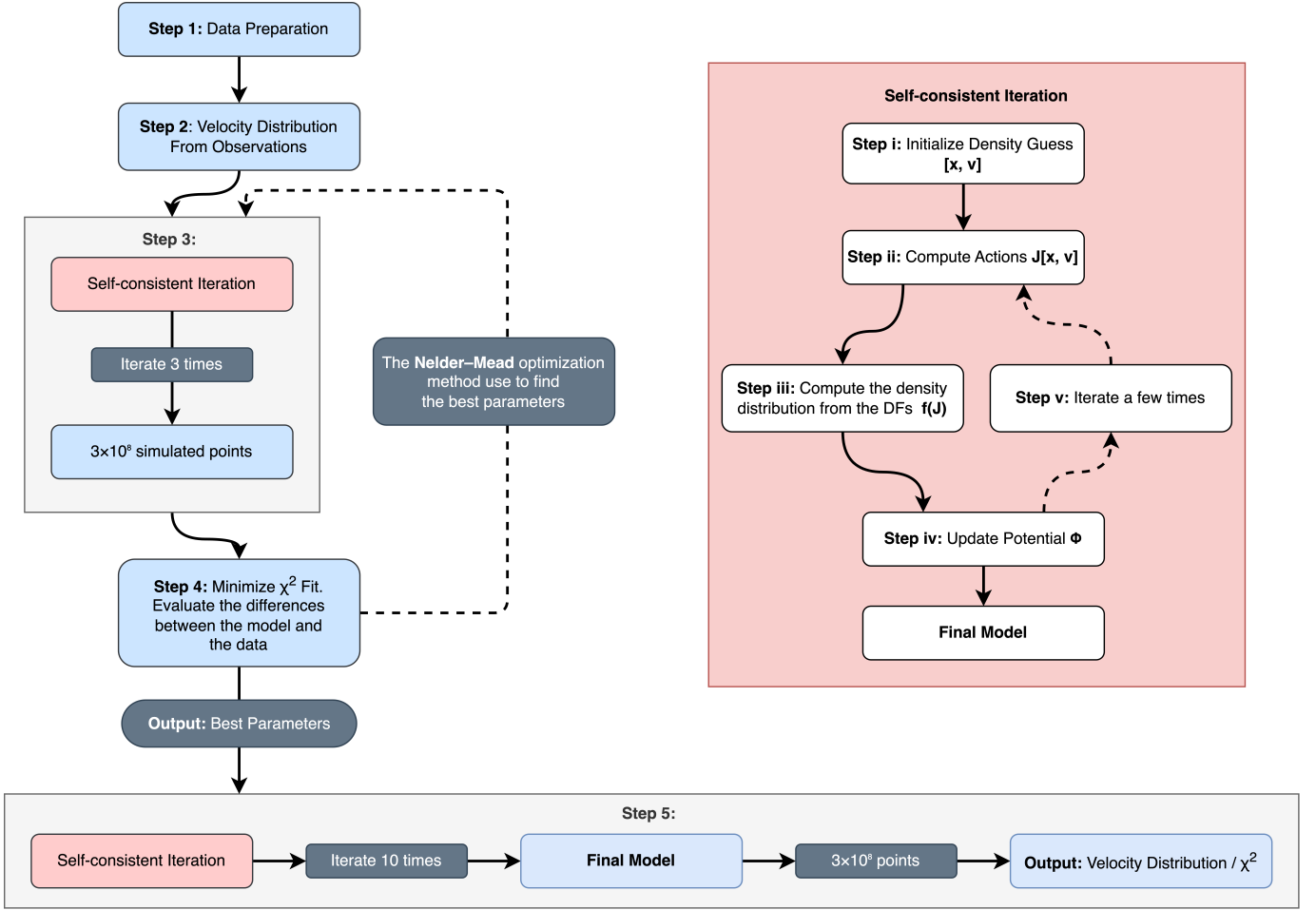


Figure 4. Flowchart for constructing the best-fitting dynamical model. The left and bottom parts are the scheme for our calculating process, while the red top-right part represents the process of building a self-consistent model using AGAMA, which is an extension of the red box on the left. The flowchart of this study consists of five stages: data preparation (Step 1), velocity distribution modeling (Step 2), self-consistent iteration (Step 3), χ^2 optimization (Step 4), and final model output (Step 5).

J_R and J_z denote radial and vertical actions, respectively. Σ , κ , and ν are azimuthal, radial, and vertical epicyclic frequencies, respectively. Σ_0 is the overall normalization of the surface density profile, consistent with the Σ_0 provided in Section 3.2. $R_c(J_\phi \equiv L_z)$, the radius for circular orbits, is a function of J_ϕ and is derived from the galactic potential.

Several parameters are specific to the DF and need to be provided in a dynamic model. σ_{r0} , R_{σ_r} , σ_{z0} , and R_{σ_z} control the radial and vertical velocity dispersion profile. σ_{r0} and σ_{z0} follow an exponential pattern with central values, while R_{σ_r} and R_{σ_z} represent radial scale length. We note that Binney & McMillan (2011) used a fixed relation $R_{\sigma_r} = R_{\sigma_z} = R_d/0.45$. However, subsequent research by Wang et al. (2017) indicated that the values of R_{σ_r} and R_{σ_z} do not maintain a fixed relationship with R_d , and are actually smaller than those estimated based on R_d .

Consequently, it was determined that the disk stars exhibited a greater degree of diffusion in velocity. In this work,

we persist in adopting $R_{\sigma_r} = R_{\sigma_z} = R_\sigma$ for the following reasons:

- (1) physically, the two parameters should not deviate significantly;
- (2) our tests with these two parameters as independent free variables demonstrate that the differences in the fit results are small;
- (3) this choice aims to reduce the number of free parameters and thus optimize computational efficiency.

The minimum velocity dispersion, σ_{\min} , is set as $\sigma_{\min} = 1\% \times (\sigma_{r0} + \sigma_{z0})/2 \text{ km s}^{-1}$ to prevent the DF from reaching unphysical values at extreme J_ϕ without radial or vertical motion, thus ensuring the physical plausibility of the model.

3.4. The contraction of dark matter halo

In addressing the modeling of the dark matter (DM) halo, this section focuses on incorporating the effect of baryonic matter contraction, which may be important for an accurate

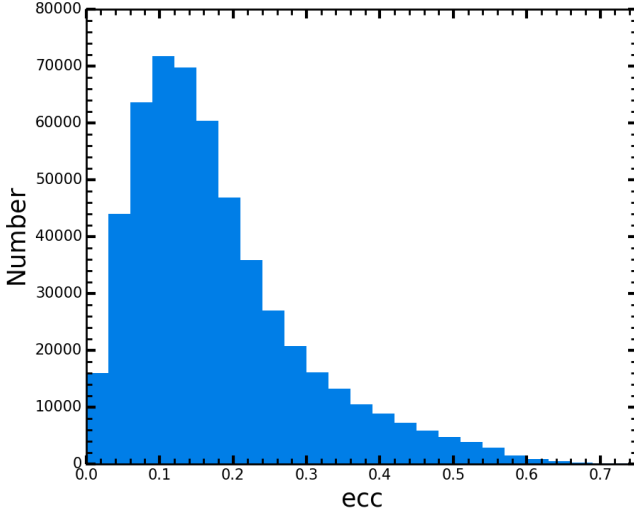


Figure 5. The distribution of recognized orbital eccentricities for 531,521 disk K giants. The horizontal axis represents the eccentricity values, while the vertical axis indicates the corresponding count of giants.

representation of the galaxy’s mass distribution within the Λ CDM cosmological framework.

Traditionally, MW mass estimates have often relied on the Navarro-Frenk-White (NFW) profile [Navarro et al. \(1997\)](#), aimed at delineating the DM distribution. This approach, however, has led to inferred halo concentrations exceeding those predicted by cosmological simulations ([Hellwing et al. 2016](#); [Klypin et al. 2016](#); [McMillan 2017](#); [Monari et al. 2018](#); [Lin & Li 2019](#)), suggesting potential inaccuracies in the halo’s depicted structure. The discrepancy primarily lies in the NFW profile’s limitations in effectively capturing the dynamic influence of baryonic matter, such as stars and gas, on the surrounding DM, especially within the inner regions of a galaxy ([Schaller et al. 2015](#); [Dutton et al. 2016](#); [Lovell et al. 2018](#)).

To mitigate this limitation, the contracted halo model proposed by [Cautun et al. \(2020\)](#) underscores the significant gravitational impact of baryonic matter on the DM distribution. The gravitational pull from the condensation of baryonic matter into stars and other structures draws in nearby DM, leading to a denser and more concentrated halo profile. This adiabatic contraction mechanism surpasses the simplistic assumptions of the NFW profile, providing a model that may accurately reflect the observed structure of the MW.

This research meticulously fits physically motivated models to the Gaia DR2 Galactic rotation curve ([Eilers et al. 2019](#)) and additional data, leveraging hydrodynamical simulations to illustrate how baryons, specifically within a radius of roughly 20 kpc, induce a notable contraction of the DM distribution. The analytical expression derived by [Cautun et al. \(2020\)](#) elucidates the relationship between the bary-

onic distribution and the consequential alteration in the DM halo profile. Notably, for the MW, this contraction significantly amplifies the enclosed DM halo mass by approximate factors of 1.3, 2, and 4 at radial distances of 20, 8, and 1 kpc, respectively, compared to an uncontracted halo, emphasizing the importance of model adjustments to rectify systematic biases in halo mass and concentration estimates due to overlooking baryonic effects.

The corrected mass is provided by the following equation ([Cautun et al. 2020](#))

$$M_{\text{DM}}(< r) = M_{\text{DM}}^{\text{DMO}}(< r)[0.45 + 0.38(\eta_{\text{bar}} + 1.16)^{0.53}], \quad (11)$$

where $\eta_{\text{bar}} = M_{\text{bar}}(< r)/M_{\text{bar}}^{\text{DMO}}(< r)$ is defined as the ratio of the baryonic masses enclosed within a specific region, as observed in hydrodynamic simulations, to those in dark matter only (DMO) simulations, and $M_{\text{bar}}^{\text{DMO}} = f_{\text{bar}} M_{\text{tot}}^{\text{DMO}}$. A value $f_{\text{bar}} = 15.7\%$ represents the cosmic mean baryon fraction according to [Planck Collaboration et al. \(2014\)](#) cosmology. In this equation, the subscript ‘DM’ refers to the mass of dark matter, ‘bar’ to the mass of baryonic matter, and ‘tot’ to the combined mass of baryonic and dark matter. The superscript ‘DMO’ denotes the mass in the context of a dark matter numerical simulation, specifically under the NFW profile. The absence of a superscript indicates the mass as described by the new model.

3.5. Circumgalactic medium

We also consider the Circumgalactic Medium (CGM) component in our study. As shown in [Cautun et al. \(2020\)](#), the CGM constitutes an extensive gas halo that surrounds a galaxy, extending hundreds of kiloparsecs beyond the visible stars and interstellar matter.

The radial density profile of the CGM has a power-law dependence on distance ([Cautun et al. 2020](#)), which can be written as:

$$\rho_{\text{CGM}} = 200\rho_{\text{crit}} A_{\text{CGM}} f_{\text{bar}} \left(\frac{r}{R_{200}} \right)^{\beta_{\text{CGM}}}, \quad (12)$$

where $\rho_{\text{crit}} = 3H_0^2/8\pi G$ denotes the Universe’s critical density, with Hubble constant $H_0 = 67.66 \text{ km s}^{-1} \text{ Mpc}^{-1}$ ([Planck Collaboration et al. 2020](#)). $A_{\text{CGM}} = 0.190$ is a normalization factor, and $\beta_{\text{CGM}} = -1.46$ is the exponent of the power-law. In addition, R_{200} is defined as the radius within which the mean density is 200 times ρ_{crit} . The mass of the CGM enclosed within a radius r is calculated as:

$$M_{\text{CGM}}(< r) = \frac{3A_{\text{CGM}}}{\beta_{\text{CGM}} + 3} f_{\text{bar}} M_{200}^{\text{tot}} \left(\frac{r}{R_{200}} \right)^{\beta_{\text{CGM}} + 3}, \quad (13)$$

where M_{200}^{tot} signifies the total mass enclosed within the halo radius R_{200} .

4. DYNAMICS OF THE MILKY WAY

4.1. Initialization parameters

We aim to find the best fitting parameters for the phase space distribution function and the density distribution so that the corresponding velocity distribution fits the observations well. Although we have made efforts to reduce unnecessary parameters, there are still as many as 15 free parameters to be determined. Given computational limitations, we decided to try using existing models and their parameters as a foundational starting point. This work involved an in-depth analysis of several established models, including those proposed by Piffl et al. (2014), Bovy (2015, MWPotential2014, hereafter Bo15), Binney & Wong (2017), McMillan (2017, hereafter Mc17), Price-Whelan (2017)¹, and Cautun et al. (2020, hereafter Ca20), with the initial distribution function parameters sourced from Wang et al. (2017). Unfortunately, most of these parameters failed to produce satisfactory results.

As a consequence, our approach focuses primarily on adjusting parameters relevant to the thin disk, thick disk, and dark matter halo, as they are the primary mass contributors to the MW. Notably, for the q parameter of the dark matter halo, after reviewing various studies (Posti & Helmi 2019; Hattori et al. 2021; Das et al. 2023; Chen et al. 2023) and our analyses, we found that the influence on our results was small. Thus, we set $q = 1$ in all our models. Since there is a significant degree of degeneracy between the distribution function parameters R_{σ_r} and R_{σ_z} , we merged these two parameters into a single parameter, R_σ .

We also took into account a detailed assessment of model reliability, including an evaluation of circular velocity near the position of the Sun and the coherence of inferred gravitational mass with established astrophysical knowledge. The culmination of these efforts was the identification and documentation of optimal model parameters, as detailed in Table 2, accompanied by the χ^2 values derived from these models, presented in Table 3.

Although the iterative DF-based technique is used to construct the self-consistent model, we do not use the DFs to name the model, but rather the initial potentials. There are three reasons. Firstly, some components, such as the two gas disks and the CGM, are fixed during the iteration. Secondly, we have arrived at the best-fitting DF models by varying the parameters in a large parameter space. Thirdly, although the final potential deviates from the initial one, the differences are small for our selected parameters.

In the case of ‘Wang17’, the results were recalculated based on its new model parameters. While some modeling details may introduce minor differences, these do not signif-

icantly impact the overall model outcomes. Additionally, it should be noted that the definition of σ_{r0} and σ_{z0} in this paper differs from that in Wang et al. (2017): their values correspond to the location of the Sun, whereas our values pertain to the Galactic Center.

4.2. Model iterations

The journey of our modeling begins with the parameters of the density and distribution functions, as shown in Table 2. These initial parameters were subjected to a thorough investigation and selection process, marking the origin of our model’s evolutionary path. Following the structured approach described by Vasiliev (2018), our model went through a series of ten iterative refinements. This iterative refinement process was designed to rapidly bring the model into self-consistency, typically achieving substantial convergence within the first three iterations.

In Figure 6, we present the results for this iterative process, tracing the evolution of the model mass distribution from its initial state to the final iteration. The upper and lower panels show the results for the ‘Mc17a’ and ‘Ca20d’ models, respectively. We note that most models undergo negligible adjustments during the iterations, with minimal changes in the upper panel. In contrast, the ‘Ca20d’ model, as depicted in the lower panel, shows a marked reduction in mass following just one iteration. This exception highlights the efficiency of our iterative process in achieving rapid convergence toward a model that reflects a self-consistent state, with significant modifications occurring after just a single iteration cycle.

Figure 7 illustrates the variation of velocity dispersion with radius before and after iteration. It can be seen that the iterations generally have a minimal impact on the velocity dispersion distribution. Therefore, the prior values in Table 2 can also serve as approximate references for the self-consistent model.

Finally, we employed Markov Chain Monte Carlo (MCMC) sampling to estimate the uncertainties in the fitted parameters. The results indicate that the model’s uncertainties are small, generally less than 10% of the parameter values. However, due to the extremely time-intensive nature of MCMC computations, specific MCMC results are not included in this paper.

4.3. Differences between models

As shown in Tables 2 and 3, after considering the proper motion distribution, the ‘Wang17’ model is no longer satisfactory. Our new model accommodates the complete velocity distribution, representing an advancement over previous studies. Our main conclusions, however, are not inconsistent with the ‘Wang17’ model. The distribution function parameters consistently suggest a hotter, more extended stellar disk, though the vertical velocity dispersion in the thin

¹ MilkyWayPotential from Gala (Price-Whelan 2017), incorporating the disk model from ‘Bo15’.

Table 2. The density and distribution function parameters of the best-fitting models are presented. The first column lists the names of the initial model parameters, where ‘Wang17’ refers to the best model described in Wang et al. (2017), ‘Mc17’ denotes the results based on McMillan (2017), with ‘Mc17a (fid)’ indicating our considered best-fitting model, and ‘Ca20’ represents the results based on Cautun et al. (2020). Other models with poorer fits are not shown here. Columns (2) to (9) list the parameters for the density models, columns (11) represents the distance from the Sun to the Galactic Center, columns (12) to (17) detail the parameters related to the distribution function, column (18) shows the circular velocity calculated at point d_{\odot} , and column (19) provides the virial mass given by the models, with a Hubble constant $H_0 = 67.66 \text{ km s}^{-1} \text{ Mpc}^{-1}$ (Planck Collaboration et al. 2020). The calculated values of the χ^2 parameter for each model are provided in Table 3. Columns (2) – (9) and (11) – (17) represent the free parameters of our model, while the last two columns show the results calculated based on the previous parameters.

Model	$\Sigma_{0,\text{thin}}$	$R_{d,\text{thin}}$	h_{thin}	$\Sigma_{0,\text{thick}}$	$R_{d,\text{thick}}$	h_{thick}	$\rho_{0,\text{halo}}$	$r_{0,\text{halo}}$
	($M_{\odot} \text{ kpc}^{-2}$)	(kpc)	(kpc)	($M_{\odot} \text{ kpc}^{-2}$)	(kpc)	(kpc)	($M_{\odot} \text{ kpc}^{-3}$)	(kpc)
(1)	(2)	(3)	(4)	(5)	(6)	(7)	(8)	(9)
Wang17	8.17e8	2.68/2.41*	0.30	2.09e8	3.31/4.07*	0.90	8.46e6	20.22
Mc17a (fid)	8.95e8	2.48	0.30	1.87e8	3.05	0.92	8.52e6	19.25
Mc17b	9.06e8	2.44	0.31	1.83e8	3.06	0.90	8.58e6	19.38
Mc17c	9.09e8	2.49	0.30	1.87e8	3.03	0.91	8.49e6	19.13
Mc17d	8.91e8	2.49	0.31	1.87e8	3.07	0.91	8.55e6	18.80
Mc17e	8.96e8	2.48	0.31	1.83e8	3.05	0.91	8.51e6	19.25
Mc17f	9.07e8	2.50	0.31	1.87e8	3.04	0.91	8.63e6	18.65
Mc17g	8.85e8	2.53	0.31	1.79e8	3.02	0.93	8.71e6	18.75
Mc17h	8.86e8	2.56	0.30	1.84e8	3.03	0.93	8.38e6	18.79
Mc17i	8.89e8	2.57	0.31	1.84e8	3.10	0.93	8.35e6	19.04
Mc17j	9.30e8	2.56	0.30	1.85e8	3.00	0.93	8.40e6	18.43
Mc17k**	9.43e8	2.36	0.31	1.90e8	3.11	1.12	8.09e6	12.48
Ca20a	1.07e9	2.39	0.31	1.16e8	3.92	0.90	1.29e7	14.00
Ca20b	1.08e9	2.46	0.31	1.14e8	3.83	0.93	1.30e7	13.74
Ca20c	1.08e9	2.45	0.31	1.16e8	3.88	0.92	1.27e7	13.83
Ca20d**	7.33e8	2.68	0.30	1.01e8	3.86	0.90	3.97e6	23.75
Ca20e**	7.37e8	2.63	0.31	1.03e8	3.86	0.92	4.05e6	22.39

* On the left are the parameters used in the density model, and on the right are the parameters used in the distribution function.

** In these models, we have employed contracted dark matter halos, see 3.4.

Model	d_{\odot}	$\sigma_{r0,\text{thin}}$	$\sigma_{z0,\text{thin}}$	$R_{\sigma,\text{thin}}$	$\sigma_{r0,\text{thick}}$	$\sigma_{z0,\text{thick}}$	$R_{\sigma,\text{thick}}$	v_{cric}	M_{200}
	(kpc)	(km s^{-1})	(km s^{-1})	(kpc)	(km s^{-1})	(km s^{-1})	(kpc)	(km s^{-1})	($\times 10^{12} M_{\odot}$)
(10)	(11)	(12)	(13)	(14)	(15)	(16)	(17)	(18)	(19)
Wang17	8.50	61.84	91.48	10.80	77.30	121.14	19.30	244.5	1.48
Mc17a (fid)	8.11	63.99	30.22	12.52	82.82	132.99	18.73	231.7	1.31
Mc17b	8.04	70.54	30.40	11.74	75.62	132.55	20.97	231.7	1.35
Mc17c	8.12	79.90	36.38	10.40	87.55	146.86	18.09	231.3	1.28
Mc17d	8.29	77.76	41.49	10.90	73.32	132.01	19.18	229.6	1.23
Mc17e	8.20	83.58	50.72	9.54	89.95	135.07	21.54	229.9	1.31
Mc17f	7.94	84.66	39.46	10.54	81.36	134.60	19.82	230.4	1.22
Mc17g	8.19	74.68	57.26	9.35	93.28	143.13	17.89	229.6	1.25
Mc17h	8.25	77.23	57.13	9.18	90.24	133.35	19.56	229.2	1.20
Mv17i	8.08	80.50	56.20	9.97	90.08	138.59	19.14	230.4	1.25
Mc17i	7.96	82.81	50.20	10.11	91.39	141.77	18.00	230.1	1.14
Mc17k**	8.40	102.94	62.66	7.64	70.79	86.20	20.96	234.3	0.41
Ca20a	8.21	103.33	93.33	8.85	204.23	331.38	4.14	229.1	0.88
Ca20b	7.90	83.19	39.88	11.01	86.48	143.28	23.04	233.2	0.85
Ca20c	8.04	86.14	35.79	9.52	255.20	367.38	5.71	230.9	0.84
Ca20d**	8.19	72.35	45.80	9.82	229.87	285.41	6.05	230.3	0.39
Ca20e**	8.12	72.88	39.48	11.18	84.81	130.09	21.99	232.8	0.84

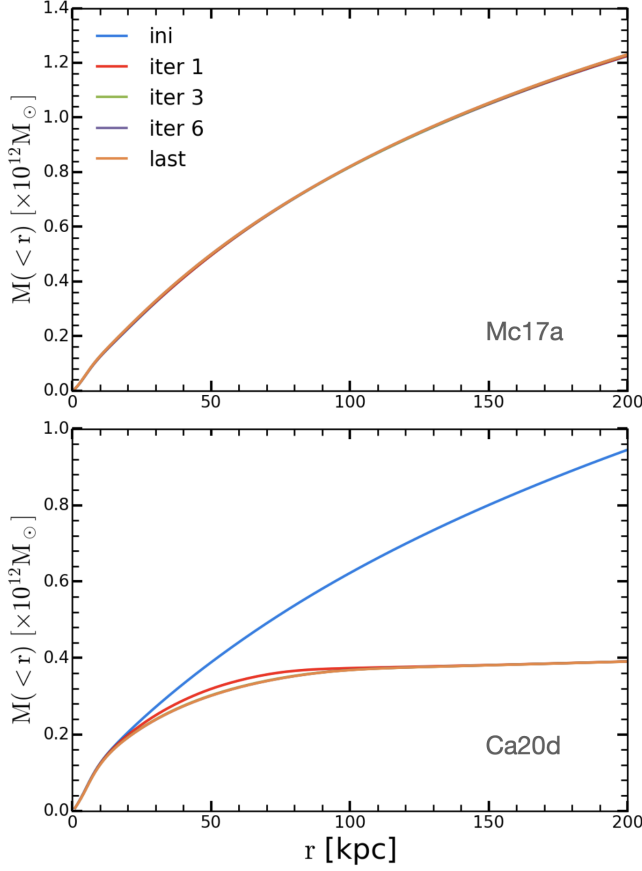


Figure 6. The mass distribution at different stages of the iteration process for the model is depicted. Various colors denote different stages of iteration, showcasing the mass distribution from the initial to the final iteration. ‘ini’ represents the model constructed with the initial parameters, and ‘last’ indicates our final model result. To avoid clutter in the visuals, we only provide the results after the 1st, 3rd, 6th, and 10th iterations. The upper panel corresponds to the ‘Mc17a’ model, where the results of multiple iterations almost overlap. The lower panel shows the results for the ‘Ca20d’ model, where three iterations are sufficient for convergence.

disk $\sigma_{z0, \text{thin}}$ is much smaller. Additionally, our model does not exclude the possibility of smaller disk models, such as ‘Ca20a’, ‘Ca20c’, and ‘Ca20d’.

For comparison purposes, Table 3 also includes the results from Binney & Vasiliev (2023, BV2023) and Binney & Vasiliev (2024, BV2024). Compared with the model in ‘BV2023’, only the bulge in ‘BV2024’ is revised. Although Binney & Vasiliev (2023) used an exponential disk DF model, which differs from the model in our study, their model can still describe our data well, particularly in the solar neighborhood. However, two factors contribute to the higher χ^2 of ‘BV2023’ model. Firstly, in the vertical direction of the Galactic disk far away from the Sun, the predicted kinematics from ‘BV2023’ and ‘BV2024’ deviate from the data significantly. Secondly, models constructed in their studies

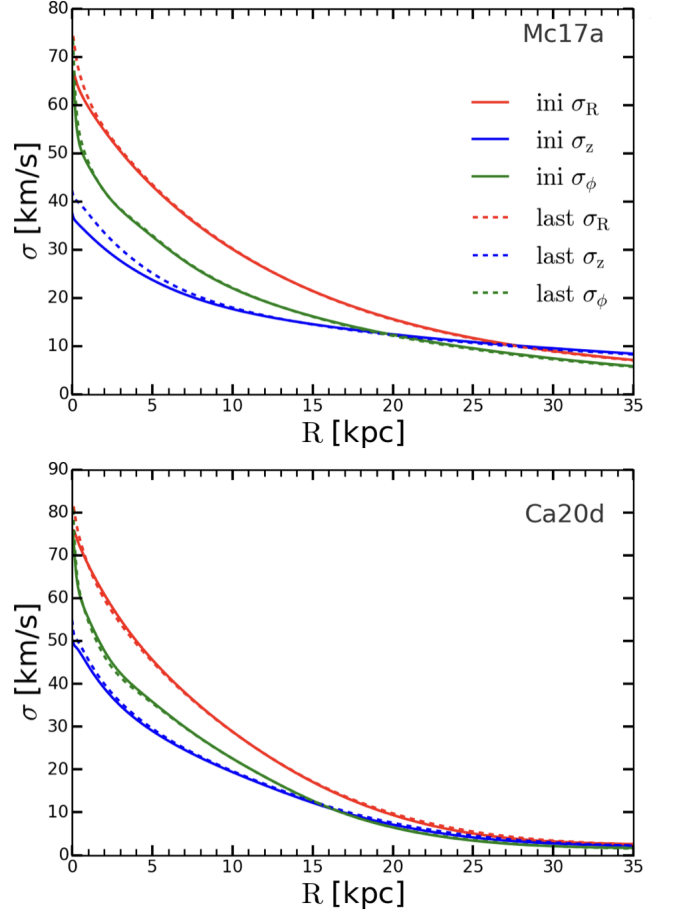


Figure 7. The variation of velocity dispersion with radius before and after iteration. The solid lines represent the initial parameter distribution, while the dashed lines indicate the distribution after iteration. Different colors represent dispersions in different directions: red for σ_R , blue for σ_z , and green for σ_ϕ . The upper panel corresponds to the ‘Mc17a’ model, while the lower panel shows the results for the ‘Ca20d’ model.

are based on giant stars with $\log g < 3.5$ and $T_{\text{eff}} < 5500$ K. We have determined that the kinematics from their giant stars are different from those of the K giant studies in this paper in some regions.

It is also worth mentioning a recent study by Robin et al. (2022), which introduced an updated ‘Besançon Galaxy Model’ (BGM). Instead of relying solely on the action J , their DF is a function of two classical integrals plus a third integral from the Stäckel approximation (E, J_ϕ, I_3). By iteratively updating the gravitational potential, they successfully constructed and refined their model. Additionally, their approach incorporates the age distribution of stars. However, their dataset is limited to more localized regions. Since their method is different from ours, we do not present χ^2 values for their model.

4.4. Best Model

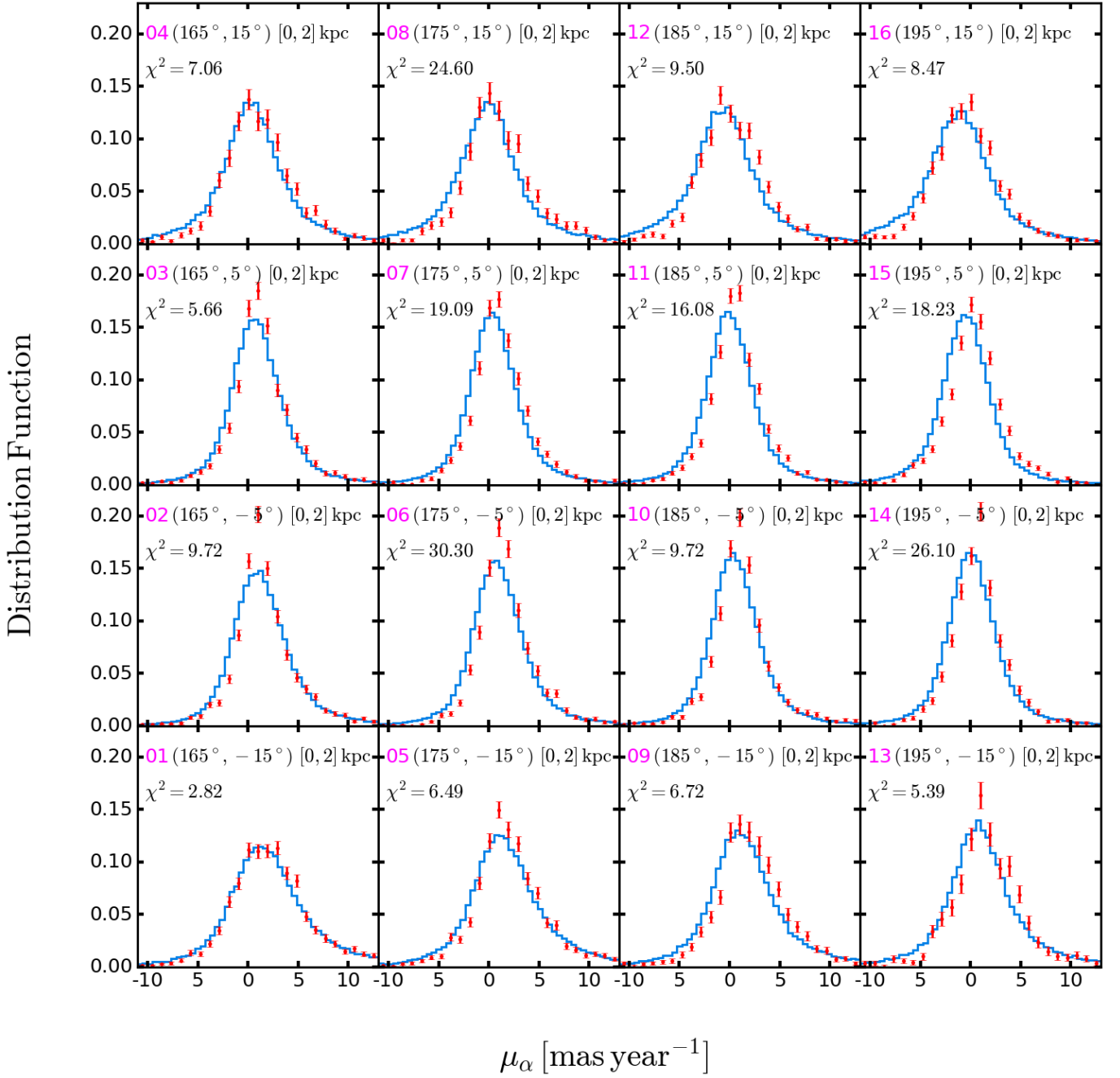


Figure 8. The probability distribution function of proper motion along the right ascension (μ_α) for sky regions 01-16, as defined in Table 1. At the top of each panel, from left to right, are the rank of the sky region, central longitude, and latitude, and the range of distances from the Sun. The blue line represents the predictions by 'Mc17a', while the red points with error bars denote the observed data and their errors. Each sky region covers an area of $10^\circ \times 10^\circ$. Notably, due to space constraints, we have displayed only one of the three observational velocity components (v_{LOS} , μ_α , μ_δ) for each set of images. Therefore, please pay careful attention to the labels on the x-axis of each figure. The reduced χ^2 is indicated in each panel.

Table 3. The reduced χ^2 values calculated by the model in Table 2. The estimation of χ_{in}^2 is derived from the first 16 sky regions as defined in Table 1, χ_{mid}^2 originates from sky regions 17-20, χ_{out}^2 is from sky regions 21-24, χ_{pole}^2 is estimated from sky regions 25-16, and χ_{tot}^2 represents the cumulative result from all sky regions. ‘dof’ stands for the degrees of freedom of the model. Compared with Table 2, two additional rows labeled ‘BV2023’ and ‘BV2024’ have been added to illustrate the differences between the best-fit models from Binney & Vasiliev (2023) and Binney & Vasiliev (2024) and the observational data presented in this study.

Model	$\chi_{\text{in}}^2/\text{dof}$	$\chi_{\text{mid}}^2/\text{dof}$	$\chi_{\text{out}}^2/\text{dof}$	$\chi_{\text{pole}}^2/\text{dof}$	$\chi_{\text{tot}}^2/\text{dof}$
Wang17	37.21	83.19	96.44	10.31	51.31
BV2023	13.58	16.34	35.63	60.64	21.02
BV2024	9.56	14.92	44.29	24.23	16.86
Mc17a (fid)	5.84	5.94	27.10	21.91	10.36
Mc17b	6.10	6.05	26.20	24.04	10.56
Mc17c	5.96	7.09	26.44	25.54	10.79
Mc17d	7.43	13.52	19.50	20.73	11.25
Mc17e	6.95	10.80	26.88	22.39	11.80
Mc17f	6.90	11.84	21.18	22.89	11.09
Mc17g	7.27	11.16	34.88	14.93	12.71
Mc17h	7.18	11.47	32.05	16.28	12.37
Mc17i	7.35	13.00	25.46	17.90	11.82
Mc17j	6.40	11.67	24.44	20.67	11.08
Mc17k*	7.44	9.94	29.93	20.68	12.30
Ca20a	12.50	27.49	61.83	8.12	22.06
Ca20b	7.91	12.78	18.87	36.55	12.55
Ca20c	6.95	8.88	28.59	42.62	13.32
Ca20d*	6.11	9.90	33.17	28.05	12.54
Ca20e*	6.08	7.36	19.92	26.44	9.97

*In these models, we have employed contracted dark matter halos, see 3.4.

We take model ‘Mc17a’ as our fiducial model because it has the smallest χ_{in}^2 when we fit the models to data in the local region. Therefore, ‘Mc17a’ model is used to illustrate our results. Due to the broad range of velocity components (v_{LOS} , μ_{α} , μ_{δ}) and sky regions, it is difficult to display all the results. Therefore, as shown in Figs. 8–12, we only present the distribution of a single randomly selected velocity component for each sky region in the main text. The complete velocity distributions from the ‘Mc17a’ model are provided in the appendix A.

The three-dimensional velocity distribution indicates that our model agrees well with the observational data from LAMOST DR8 and Gaia EDR3. However, the fit for the v_{LOS} is better than for the proper motion μ_{α} and μ_{δ} , with the average χ^2 values for the proper motion being 2-5 times higher than those for the v_{LOS} . This discrepancy is especially pronounced in regions farther from the Sun. The discrepancy may also indicate that there are still some systematic errors

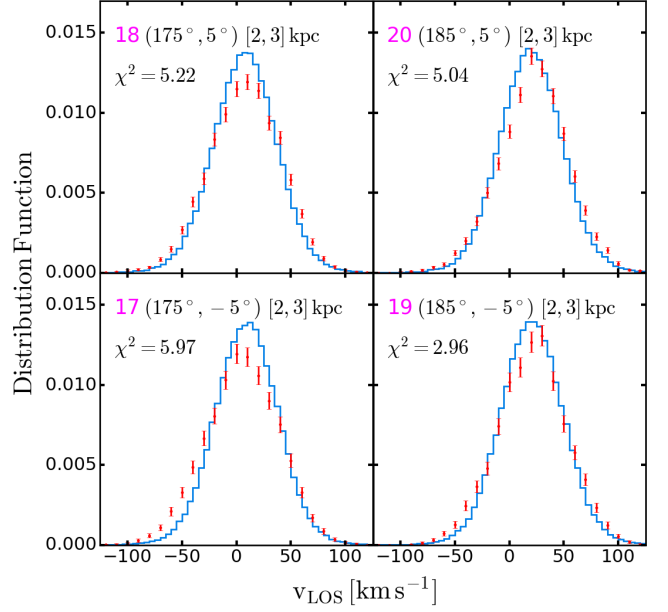


Figure 9. The probability distribution function of the line-of-sight velocity (v_{LOS}) for sky regions 17-20, as defined in Table 1. Each sky region covers an area of $10^\circ \times 10^\circ$.

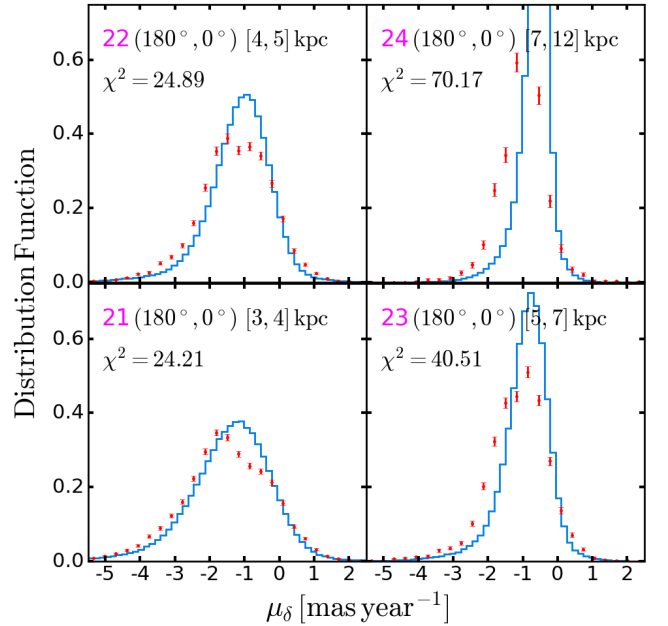


Figure 10. The probability distribution function of proper motion in the declination direction (μ_{δ}) for sky regions 21-24, as defined in Table 1. Each sky region covers an area of $20^\circ \times 20^\circ$.

in the v_{LOS} measurements from LAMOST and the proper motion measurements from Gaia.

Figs. 8–9 show that the fitting results for the three velocity components in regions 01-20 are fairly accurate. Some observational values are unusually high compared to the model (e.g., region 10 in Figure 8), and systematic offsets are visi-

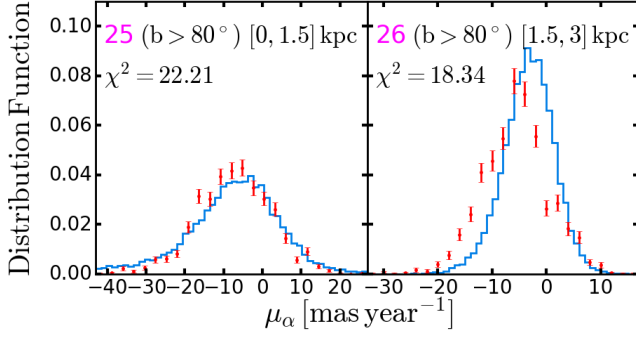


Figure 11. The right ascension direction proper motion (μ_α) probability distribution function for sky regions 25 and 26, as defined in Table 1. Each sky region covers a circle with a diameter of 10° .

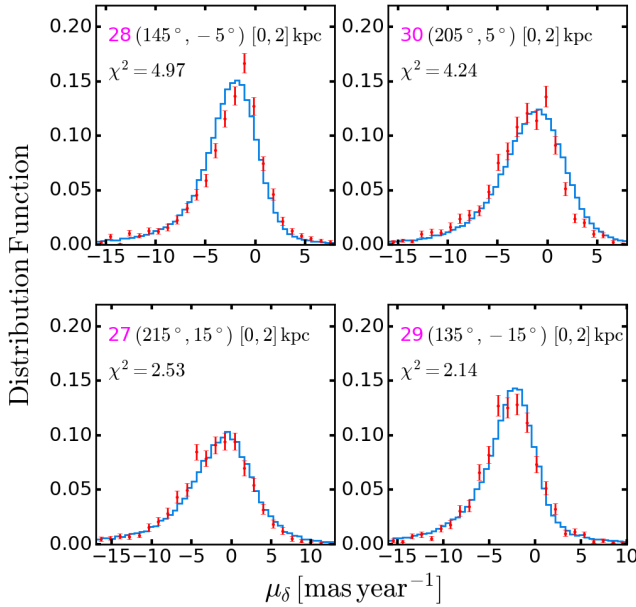


Figure 12. The probability distribution function of proper motion in the declination direction (μ_δ) for sky regions 27-30, as defined in Table 1. Each sky region covers an area of $10^\circ \times 10^\circ$.

ble in certain areas (e.g., region 15 in Figure 8 and Figure 9). This may be due to the influence of anomalous small-scale structures. Queries of relevant catalogs for these regions did not reveal any globular clusters (Sun et al. 2023). However, some bright open clusters and spiral arm structures (Wenger et al. 2000; Tarricq et al. 2021; Poggio et al. 2021; Hao et al. 2021; Pang et al. 2022; Fu et al. 2022) may have caused anomalous peaks in certain sky regions. For example, several nearby regions (< 2 kpc) close to the Galactic plane (such as regions 02, 03, and 14) include the Local Spiral arm. More distant regions are also influenced by the Perseus Arm. Additionally, after excluding several K giants associated with open clusters in these regions, this issue was partially alleviated.

In regions farther from the Sun, for example for the anti-Galactic centre direction, as shown in Figure 10. The fitting performance deteriorates, indicating that our model struggles to describe these distant regions accurately. Although the χ^2 values for these regions, as shown in Table 3, are as poor as those for the North Galactic Pole, some models, such as ‘Ca20a’, still provide a reasonable fit. None of our attempts could produce an acceptable fit for sky region 24 (Top right panel).

Figure 11 illustrates the distribution of μ_δ for giants in sky regions 25 and 26. Given that we have set $R_{\sigma_r} = R_{\sigma_z}$, the fit for results perpendicular to the Galactic plane is acceptable. However, compared to the radial regions, the fit for proper motion data in the vertical direction seems to be better than that for v_{LOS} , although the difference is not substantial.

Finally, Figure 12 provides a general test of our model by selecting four regions with relatively complete data coverage from different directions, focusing on giants near the Sun. The results indicate that our model performs reliably in regions close to the Sun.

4.5. Predictions of the models

In this section, we focus on three selected models for detailed analysis. In addition to our fiducial model ‘Mc17a’, we also consider the ‘Ca20d’ and ‘Ca20e’ models. ‘Ca20d’ has the smallest virial mass of among the models shown in Table 3, and ‘Ca20e’ demonstrates the best overall fit compared to all other models.

Figure 13 illustrates the mid-plane density distributions of all the components. The black lines represent the two stellar disks; the blue lines denote the two spherical structures, the dark matter halo and the bulge; the red lines correspond to the two gas disks; and the green lines indicate the CGM. Notably, ‘Mc17a’ does not include the CGM structure. It may be seen that the density distributions of the three models do not demonstrate significant differences. Each component’s distribution is approximately exponential, and in the vicinity of the Sun, the primary contributions arise from the thin disk and HI gas, with their density contributions being roughly 2-3 times that of the dark halo.

Figure 14 shows the density distributions as a function of the vertical height at the solar radius. The color scheme is consistent with that of Figure 13. The distribution differences between the three models are not substantial. The dark halo and CGM are depicted as nearly horizontal in the figure. Additionally, in the ‘Mc17a’ model, the density of the thin disk decreases more rapidly in the z -direction compared to the other two models.

Table 4 presents the densities of the different components of the MW at the position of the Sun. The stellar density (thin disk plus thick disk) in our fiducial model is $0.0696 \text{ M}_\odot \text{ pc}^{-3}$, which is twice the value $0.0317 \text{ M}_\odot \text{ pc}^{-3}$

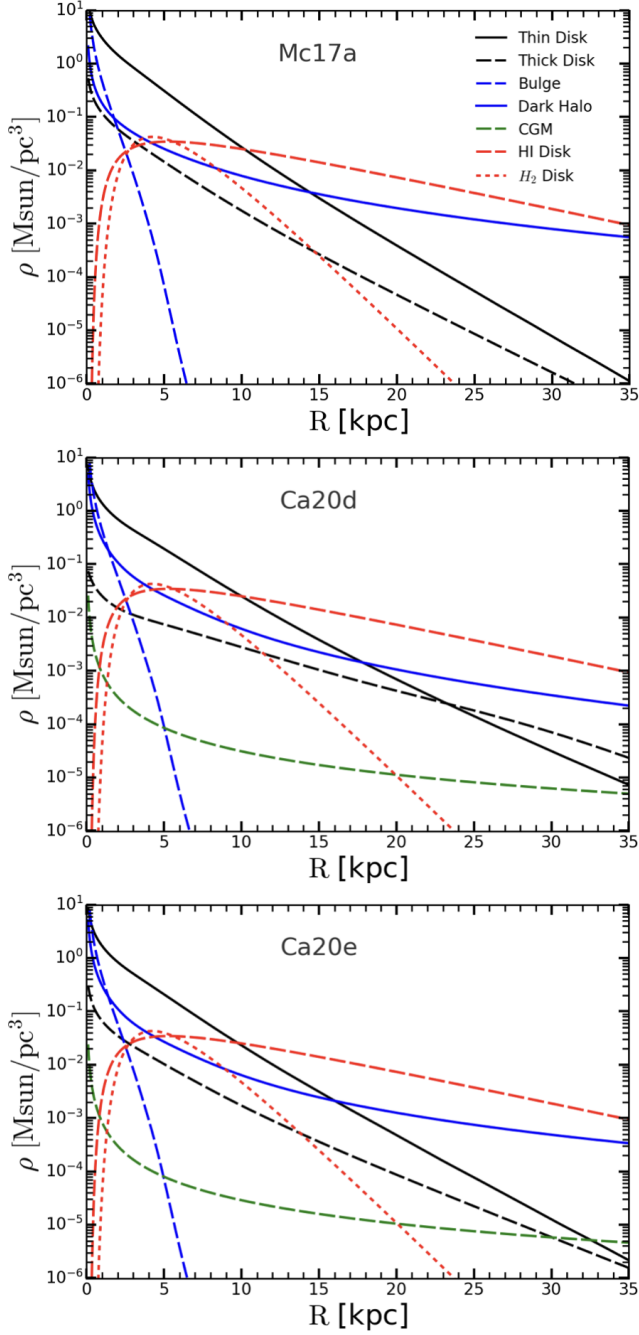


Figure 13. Mid-plane density distributions of various components. The black solid and dashed lines denote the thin and thick disks, respectively. The blue solid and dashed lines represent the results for the dark matter halo and bulge, respectively. The red long-dashed line denotes the HI gas disk, the red short-dashed line denotes the H_2 gas disk, and the green dashed line denotes the CGM. From top to bottom, the results are for ‘Mc17a’, ‘Ca20d’, and ‘Ca20e’ models.

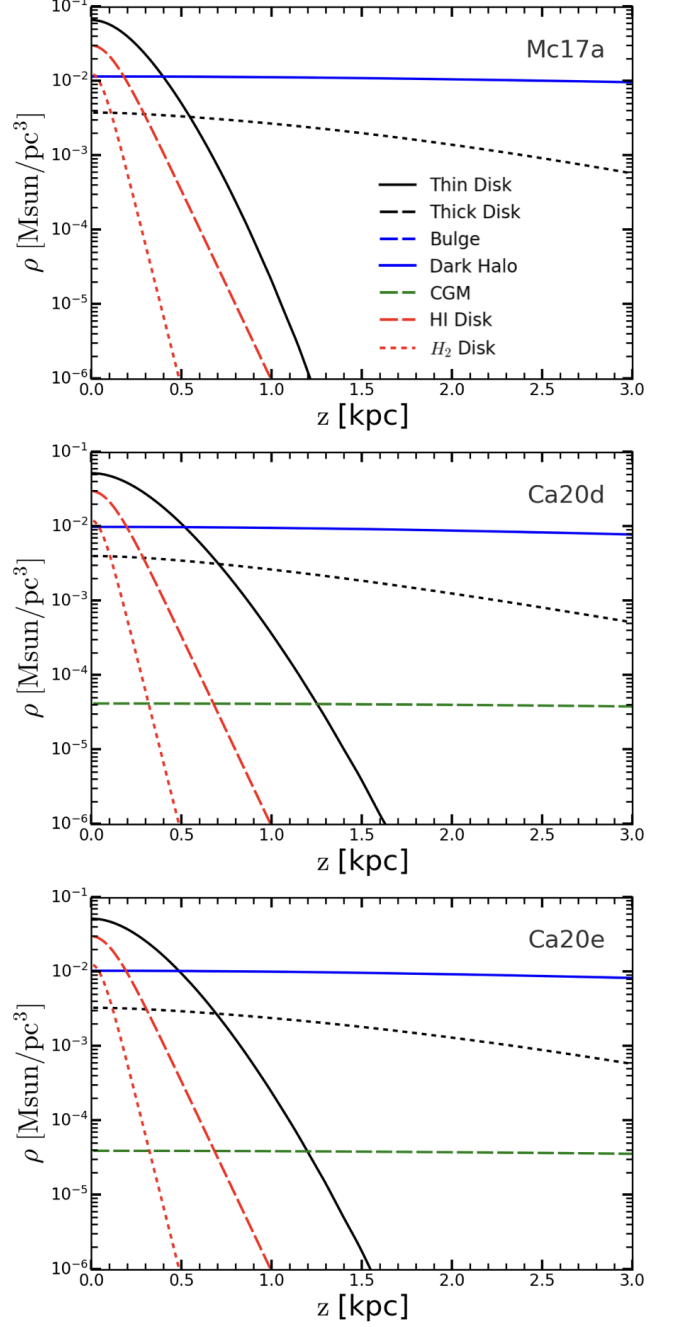


Figure 14. Similar to Figure 13, but for the density distributions along the height at the Solar Position (d_\odot).

in ‘BV2023’ obtained using the data from Gaia DR2, while it is close to the results $0.0594 \pm 0.0008 \text{ M}_\odot \text{ pc}^{-3}$ obtained by using the main-sequence turnoff and subgiant stars from the LAMOST surveys (Xiang et al. 2018). However, the local dark matter density $0.0115 \text{ M}_\odot \text{ pc}^{-3}$ is consistent with the different studies (e.g. McMillan 2017; Guo et al. 2020; Robin et al. 2022; Binney & Vasiliev 2023; Lim et al. 2025).

Table 4. Densities for different models in $M_{\odot}\text{pc}^{-3}$.

Model	Thin Disk	Thick Disk	Dark Halo	HI Disk	H_2 Disk
Mc17a	0.0658	0.0038	0.0115	0.0297	0.0120
Ca20d	0.0517	0.0040	0.0098	0.0297	0.0120
Ca20e	0.0515	0.0033	0.0103	0.0299	0.0124

In Figure 15, we show the velocity dispersions for the three models with only the results of the two stellar disks, the dark matter halo, and the bulge being presented. It is noted that the radial velocity dispersion of the thin disk is smaller than that of the thick disk, except in the ‘Ca20d’ model beyond 20 kpc. Although the radial velocity dispersion from the thick disk in the ‘Ca20d’ model is highest near the Galactic center, it decreases rapidly with increasing radius. Additionally, the velocity dispersions (σ_R , σ_z , σ_ϕ) of the bulge in the central regions ($R < 3$ kpc) are larger than those from the thick disk for the ‘Mc17a’ and ‘Ca20e’ models, while the opposite is true for the ‘Ca20d’ model.

Figure 16 illustrates the surface density distributions of disk stars for the three models. In all three, the surface density decreases exponentially with radius. The black dashed line in the figure indicates a scale length of 3 kpc, which closely matches the declining trends of the models ‘Ca20d’ and ‘Ca20e’. This scale length is slightly smaller than the $R_d = 3.6$ kpc reported by Binney & Vasiliev (2024). Conversely, model ‘Mc17a’ exhibits a more rapid decrease in surface density, resulting in a correspondingly larger scale length.

There is considerable variation in the estimated virial mass of the MW across the different models, with the mass ranging from 0.39 to $1.31 \times 10^{12} M_{\odot}$. The initial parameters of the ‘Ca20’ model are not significantly different from those of ‘Mc17’. The primary difference between these models is the inclusion of a CGM component in ‘Ca20’, which is absent in ‘Mc17’. The fitting results suggest that incorporating the CGM component favors a smaller $r_{0,\text{halo}}$, leading to a reduced mass in the outer regions of the model, and consequently, a smaller estimated virial mass for the MW.

The black solid lines in Figure 17 show the circular velocity curves for the gravitational potentials of the three models, ‘Mc17a’, ‘Ca20d’ and ‘Ca20e’. All models agree well with the observational data points in the local region, which includes measurements by Eilers et al. (2019) using 23,000 red giant stars, Abhimit et al. (2020) using three-dimensional velocity vectors of classical Cepheids, and Wang et al. (2023) calculations of circular velocities based on Gaia DR3.

With similar distributions of baryonic matter, the ‘Ca20d’ and ‘Ca20e’ models align better with observations of circular velocity in regions far from the Galactic center. However, the masses predicted by the two models ‘Mc17a’ and ‘Ca20d’ in

Table 2 differ by more than a factor of three, indicating that the distribution of dark matter is a critical factor influencing the total mass of a galaxy. Compared to the classical NFW profile, a contracted dark matter halo (Cautun et al. 2020) can significantly reduce the estimated galactic mass while maintaining similar mass in the inner regions.

However, most current studies estimating the mass of the MW rely on extrapolations based on the NFW model (Watkins et al. 2010; Vasiliev 2019b; Wang et al. 2020; Sun et al. 2023). Non-model-dependent constraints on the MW’s mass are typically reliable within 60 kpc (Vasiliev 2019b; Fritz et al. 2020; Sun et al. 2023). From the circular velocity curve of ‘Ca20d’, the MW’s M_{200} could be as low as $0.4 \times 10^{12} M_{\odot}$, which is consistent with the result of Bird et al. (2022b).

Figure 18 shows the mean streaming velocities of the thin and thick disks at mid-plane. The thin disk exhibits significantly higher velocities compared to the thick disk. Furthermore, as the distance from the Galactic center increases, the velocity dispersion decreases, and the mean stream velocity slightly surpasses the circular velocity.

4.6. A hotter outer disk

It seems that all the models in Table 3 fail to fit well the outer regions of the MW. The velocities predicted by all models are narrower than those observed at distances far from the Galactic center. This suggests that the MW outer disk, at least within the range of 15–20 kpc from the Galactic center, is hotter than any of the models we mentioned here. It is known that the outer disk is flared and warped (Mackereth et al. 2019; Abhimit et al. 2020; Sun et al. 2024). Moreover, the vertical velocity dispersion in the outer disk does not decline with the radius; instead, it slightly increases with the radius beyond 12 kpc from the Galactic center (Sanders & Das 2018; Mackereth et al. 2019).

Furthermore, we have also attempted to introduce a new disk model. This model, however, does not significantly improve the results, possibly due to the complexity introduced by too many free parameters, making it difficult to achieve a global minimum. Although we did not adopt a three-disk model, we advocate for a new structure with larger velocity dispersions in the outer MW, as existing models cannot provide satisfactory results for the entire velocity distribution. Additionally, the resonant effects of the Galactic bar (Binney 2020; Chiba & Schönrich 2021; Moreno et al. 2021), along with certain non-equilibrium structures in the MW, such as phase spirals, may influence the observed velocity distribution (Xu et al. 2020; Guo et al. 2022; McMillan et al. 2022; Guo et al. 2024).

5. CONCLUSIONS

This study presents a comprehensive dynamical model of the Milky Way (MW), utilizing an extensive dataset of

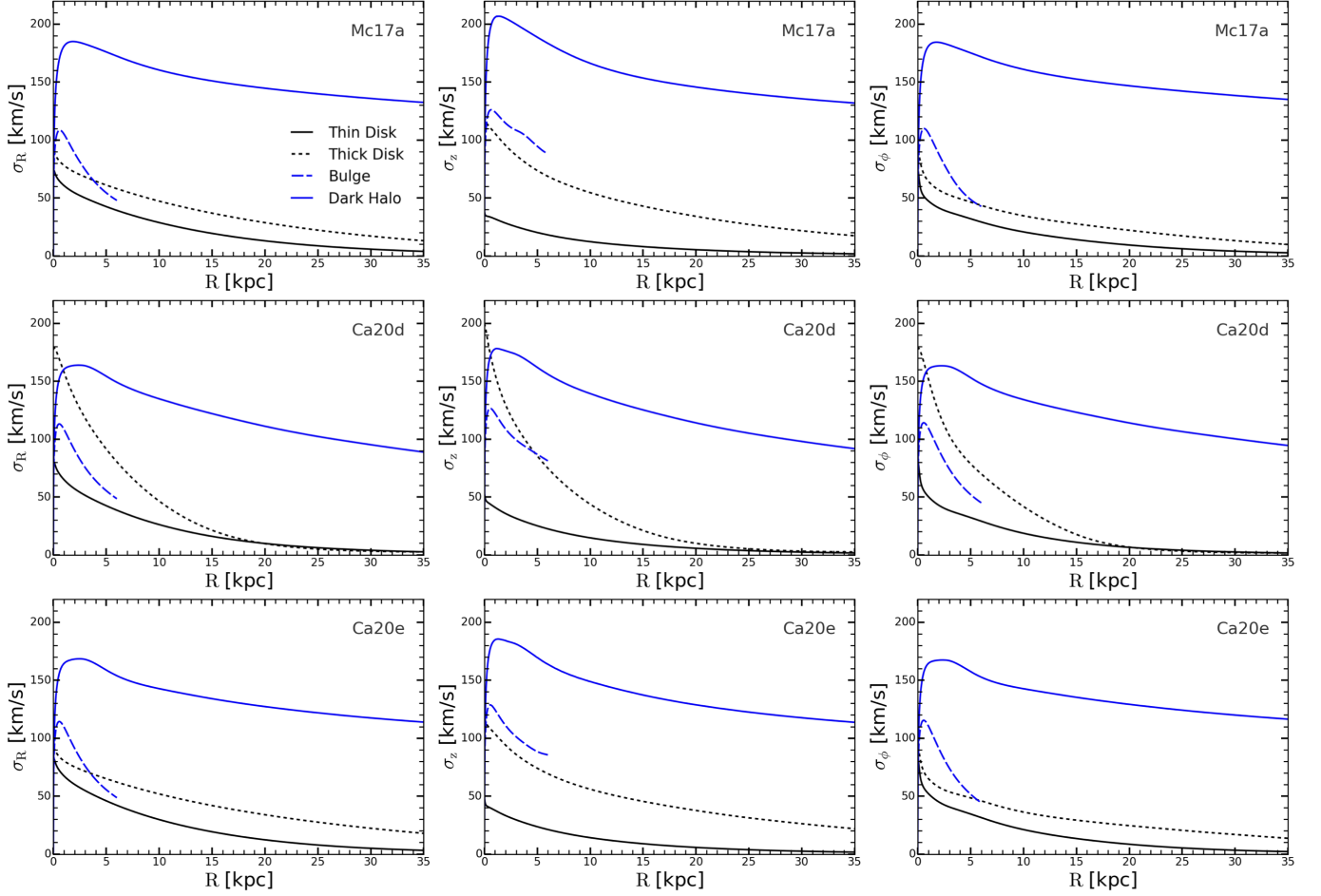


Figure 15. From left to right, the radial distributions of the velocity dispersions σ_R , σ_z , and σ_ϕ are presented. The color scheme is consistent with that used in Figure 13. The black solid line denotes the thin disk, the black dashed line denotes the thick disk, the blue solid line denotes the dark matter halo, the blue dashed line denotes the bulge and reach only to $R = 6$ kpc. The upper panel corresponds to the ‘Mc17a’ model, the middle panel shows the results for the ‘Ca20d’ model, while the lower panel shows the results for the ‘Ca20e’ model.

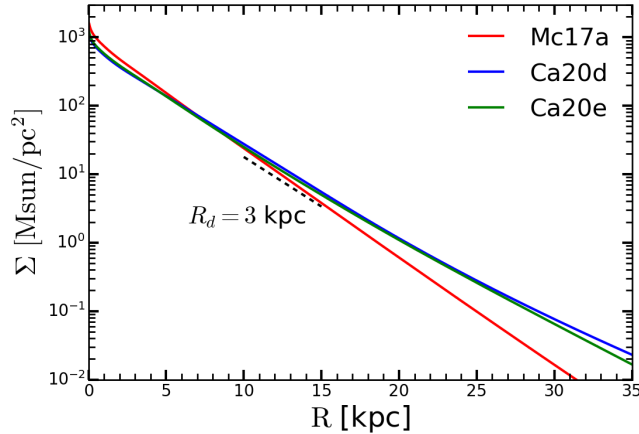


Figure 16. Surface density distribution of disk stars for different models. The red, blue and green lines are the results for ‘Mc17a’, ‘Ca20d’ and ‘Ca20e’ models, respectively.

86,109 K-type giant stars. The combination of observational data from LAMOST DR8 and Gaia EDR3 provides a robust

foundation for analyzing the kinematic and spatial distribution of these stars within the Galactic disk.

Through careful data selection and the application of complex modeling techniques, we construct the best self-consistent model of the MW we can achieve. The main results of this paper can be summarized as follows.

(i) Our study employs an action-based modeling approach, incorporating both the circumgalactic medium (CGM) and a contracted dark matter halo into our models. By experimenting with multiple initial parameter sets, we explore a broader parameter space and identify the model parameters that best match our observational data.

(ii) Compared to the work of Wang et al. (2017), we have not only updated the modeling methodology but have also utilized a new and more comprehensive observational dataset. The spatial distribution of the new K giants data is significantly more complete, allowing us to model the full three-dimensional velocity distribution of the K giants, thereby ensuring more precise constraints on the models.

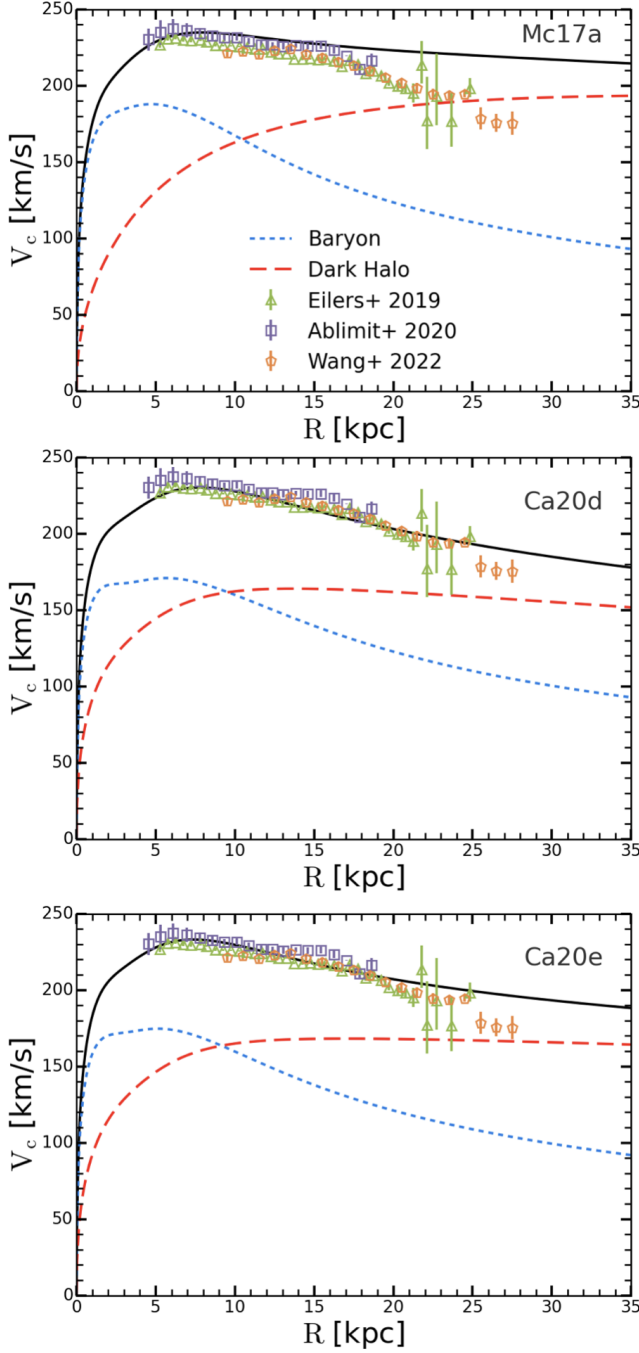


Figure 17. Distributions of the circular velocity with radius generated by the stellar and gas baryonic matter (blue dashed), the dark matter halo (red long-dashed), and the total circular velocity (black solid). The data points represent recent estimates of V_c based on three studies using different tracers. From top to bottom, the results are for ‘Mc17a’, ‘Ca20d’, and ‘Ca20e’ models, respectively.

(iii) The majority of our model parameters support a hotter and more extended thick disk (larger $\sigma_{z0, \text{thick}}$ and $R_{\sigma, \text{thin}}$), which aligns with the conclusions of Wang et al. (2017). However, we also highlight that small thick disks ($R_{\sigma, \text{thick}}$)

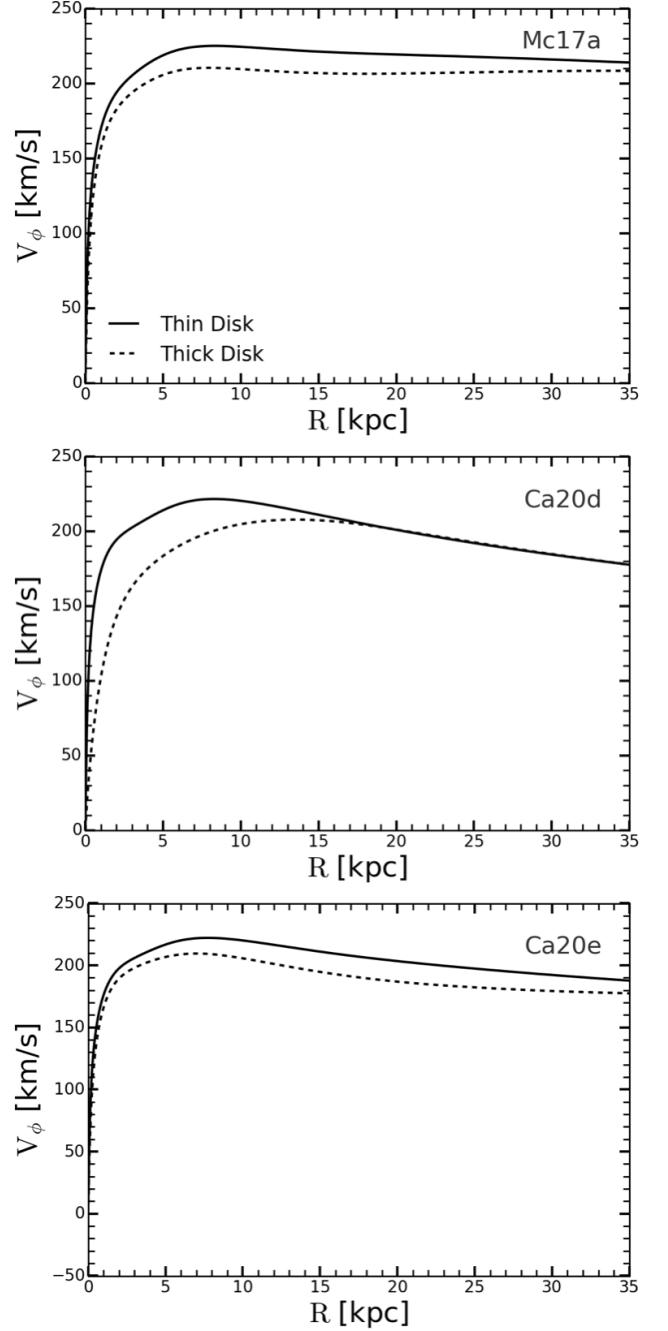


Figure 18. Mean streaming velocities of the thick (solid lines) and the thin disk (dashed lines) in the mid-plane for different Models.

cannot be entirely ruled out. Additionally, the thin disk is generally found to be thinner and cooler (smaller $\sigma_{z0, \text{thin}}$).

(iv) Our best-fitting model indicates that the velocity distribution of K giants near the Sun is consistent with the predictions of our dynamical model. However, there is still a discrepancy between the proper motion distributions of the model and data in regions far from the Galactic center. This indicates that the structure of the MW is more complex than

we thought. This might require the introduction of new structures to explain these discrepancies, such as additional disks or spiral arms, or an assumption of non-axisymmetry. In particular, the presence of the Galactic bar (Binney 2020; Chiba & Schönrich 2021; Moreno et al. 2021), and non-equilibrium features (e.g., phase spirals) (Xu et al. 2020; Guo et al. 2022; McMillan et al. 2022; Guo et al. 2024) could play significant roles.

Here, we have attempted to construct a self-consistent model of the MW, which can fit the observed kinematics in the regions near and far from the Sun. Although we have found a best-fitting model from exploring a large parameter space, a discrepancy between the model and the data still exists, which indicates the real MW is more complex than the model we adopt here. Future work should expand upon these results by enlarging the dataset and refining the model to accommodate additional complexities, such as non-axisymmetric components and external perturbations.

ACKNOWLEDGMENTS

We thank the referees for the constructive and detailed comments for improving the paper. We are grateful to

Chao Liu for the helpful discussion. This work is partly supported by the NSFC International (Regional) Cooperation and Exchange Project (No. 12361141814), by the National Key Research and Development Program of China (No. 2018YFA0404501 to Shude Mao, 2023YFB3002501 to Q. Wang), and by the National Science Foundation of China (Grant No. 11821303 to Shude Mao). We also acknowledge the science research grants from the China Manned Space Project with No. CMS-CSST-2021-A11. Q. Wang is also supported by the Strategic Priority Research Program of Chinese Academy of Sciences, Grant No. XDB0500203, SKA Program of China (Grant number 2020SKA0110401), National Natural Science Foundation of China (Grant numbers 11988101, 12033008), and K.C.Wong Education Foundation. Y. Li and X. Zhang acknowledge financial support from the National Natural Science Foundation of China (Grant numbers 12473091, 12473001).

Facilities: LAMOST, Gaia

Software: Astropy (Astropy Collaboration et al. 2013, 2018), AGAMA (Vasiliev 2018)

REFERENCES

- Ablimit, I., Zhao, G., Flynn, C., & Bird, S. A. 2020, *Astrophysical Journal Letters*, 895, L12, doi: [10.3847/2041-8213/ab8d45](https://doi.org/10.3847/2041-8213/ab8d45)
- Anguiano, B., Majewski, S. R., Allende Prieto, C., et al. 2018, *Astronomy and Astrophysics*, 620, A76, doi: [10.1051/0004-6361/201833387](https://doi.org/10.1051/0004-6361/201833387)
- Anguiano, B., Majewski, S. R., Hayes, C. R., et al. 2020, *The Astronomical Journal*, 160, 43, doi: [10.3847/1538-3881/ab9813](https://doi.org/10.3847/1538-3881/ab9813)
- Astraatmadja, T. L., & Bailer-Jones, C. A. L. 2016, *The Astrophysical Journal*, 832, 137, doi: [10.3847/0004-637X/832/2/137](https://doi.org/10.3847/0004-637X/832/2/137)
- Astropy Collaboration, Robitaille, T. P., Tollerud, E. J., et al. 2013, *Astronomy and Astrophysics*, 558, A33, doi: [10.1051/0004-6361/201322068](https://doi.org/10.1051/0004-6361/201322068)
- Astropy Collaboration, Price-Whelan, A. M., Sipőcz, B. M., et al. 2018, *The Astronomical Journal*, 156, 123, doi: [10.3847/1538-3881/aabc4f](https://doi.org/10.3847/1538-3881/aabc4f)
- Bennett, M., & Bovy, J. 2019, *Monthly Notices of the Royal Astronomical Society*, 482, 1417, doi: [10.1093/mnras/sty2813](https://doi.org/10.1093/mnras/sty2813)
- Binney, J. 2010, *Monthly Notices of the Royal Astronomical Society*, 401, 2318, doi: [10.1111/j.1365-2966.2009.15845.x](https://doi.org/10.1111/j.1365-2966.2009.15845.x)
- . 2012, *Monthly Notices of the Royal Astronomical Society*, 426, 1328, doi: [10.1111/j.1365-2966.2012.21692.x](https://doi.org/10.1111/j.1365-2966.2012.21692.x)
- Binney, J. 2018, in *Astrometry and Astrophysics in the Gaia Sky*, ed. A. Recio-Blanco, P. de Laverny, A. G. A. Brown, & T. Prusti, Vol. 330, 111–118, doi: [10.1017/S1743921317007049](https://doi.org/10.1017/S1743921317007049)
- . 2020, *Monthly Notices of the Royal Astronomical Society*, 495, 895, doi: [10.1093/mnras/staa1103](https://doi.org/10.1093/mnras/staa1103)
- Binney, J., & Kumar, S. 1993, *Monthly Notices of the Royal Astronomical Society*, 261, 584, doi: [10.1093/mnras/261.3.584](https://doi.org/10.1093/mnras/261.3.584)
- Binney, J., & McMillan, P. 2011, *Monthly Notices of the Royal Astronomical Society*, 413, 1889, doi: [10.1111/j.1365-2966.2011.18268.x](https://doi.org/10.1111/j.1365-2966.2011.18268.x)
- Binney, J., & McMillan, P. J. 2016, *Monthly Notices of the Royal Astronomical Society*, 456, 1982, doi: [10.1093/mnras/stv2734](https://doi.org/10.1093/mnras/stv2734)
- Binney, J., & Sanders, J. L. 2014, in *Setting the scene for Gaia and LAMOST*, ed. S. Feltzing, G. Zhao, N. A. Walton, & P. Whitelock, Vol. 298, 117–129, doi: [10.1017/S1743921313006297](https://doi.org/10.1017/S1743921313006297)
- Binney, J., & Tremaine, S. 2008, *Galactic Dynamics: Second Edition*
- Binney, J., & Vasiliev, E. 2023, *Monthly Notices of the Royal Astronomical Society*, 520, 1832, doi: [10.1093/mnras/stad094](https://doi.org/10.1093/mnras/stad094)
- . 2024, *Monthly Notices of the Royal Astronomical Society*, 527, 1915, doi: [10.1093/mnras/stad3312](https://doi.org/10.1093/mnras/stad3312)
- Binney, J., & Wong, L. K. 2017, *Monthly Notices of the Royal Astronomical Society*, 467, 2446, doi: [10.1093/mnras/stx234](https://doi.org/10.1093/mnras/stx234)
- Bird, S. A., Xue, X.-X., Liu, C., et al. 2022a, *Monthly Notices of the Royal Astronomical Society*, 516, 731, doi: [10.1093/mnras/stac2036](https://doi.org/10.1093/mnras/stac2036)
- . 2022b, *Monthly Notices of the Royal Astronomical Society*, 516, 731, doi: [10.1093/mnras/stac2036](https://doi.org/10.1093/mnras/stac2036)

- Bovy, J. 2015, *The Astrophysical Journal Supplement Series*, 216, 29, doi: [10.1088/0067-0049/216/2/29](https://doi.org/10.1088/0067-0049/216/2/29)
- Carlin, J. L., Liu, C., Newberg, H. J., et al. 2015, *The Astronomical Journal*, 150, 4, doi: [10.1088/0004-6256/150/1/4](https://doi.org/10.1088/0004-6256/150/1/4)
- Cautun, M., Benítez-Llambay, A., Deason, A. J., et al. 2020, *Monthly Notices of the Royal Astronomical Society*, 494, 4291, doi: [10.1093/mnras/staa1017](https://doi.org/10.1093/mnras/staa1017)
- Chen, A., Li, Z., Wang, Y., et al. 2023, *Monthly Notices of the Royal Astronomical Society*, 525, 3075, doi: [10.1093/mnras/stad2296](https://doi.org/10.1093/mnras/stad2296)
- Chiba, R., & Schönrich, R. 2021, *Monthly Notices of the Royal Astronomical Society*, 505, 2412, doi: [10.1093/mnras/stab1094](https://doi.org/10.1093/mnras/stab1094)
- Das, M., Ianjamasimanana, R., McGaugh, S. S., Schombert, J., & Dwarakanath, K. S. 2023, *Astrophysical Journal Letters*, 946, L8, doi: [10.3847/2041-8213/acc10e](https://doi.org/10.3847/2041-8213/acc10e)
- Deng, L.-C., Newberg, H. J., Liu, C., et al. 2012, *Research in Astronomy and Astrophysics*, 12, 735, doi: [10.1088/1674-4527/12/7/003](https://doi.org/10.1088/1674-4527/12/7/003)
- Ding, P.-J., Xue, X.-X., Yang, C., et al. 2021, *The Astronomical Journal*, 162, 112, doi: [10.3847/1538-3881/ac0892](https://doi.org/10.3847/1538-3881/ac0892)
- Dutton, A. A., Macciò, A. V., Dekel, A., et al. 2016, *Monthly Notices of the Royal Astronomical Society*, 461, 2658, doi: [10.1093/mnras/stw1537](https://doi.org/10.1093/mnras/stw1537)
- Eilers, A.-C., Hogg, D. W., Rix, H.-W., & Ness, M. K. 2019, *The Astrophysical Journal*, 871, 120, doi: [10.3847/1538-4357/aaf648](https://doi.org/10.3847/1538-4357/aaf648)
- Fritz, T. K., Di Cintio, A., Battaglia, G., Brook, C., & Taibi, S. 2020, *Monthly Notices of the Royal Astronomical Society*, 494, 5178, doi: [10.1093/mnras/staa1040](https://doi.org/10.1093/mnras/staa1040)
- Fu, X., Bragaglia, A., Liu, C., et al. 2022, *Astronomy and Astrophysics*, 668, A4, doi: [10.1051/0004-6361/202243590](https://doi.org/10.1051/0004-6361/202243590)
- Gaia Collaboration, Prusti, T., de Bruijne, J. H. J., et al. 2016, *Astronomy and Astrophysics*, 595, A1, doi: [10.1051/0004-6361/201629272](https://doi.org/10.1051/0004-6361/201629272)
- Gaia Collaboration, Brown, A. G. A., Vallenari, A., et al. 2018, *Astronomy and Astrophysics*, 616, A1, doi: [10.1051/0004-6361/201833051](https://doi.org/10.1051/0004-6361/201833051)
- . 2021, *Astronomy and Astrophysics*, 649, A1, doi: [10.1051/0004-6361/202039657](https://doi.org/10.1051/0004-6361/202039657)
- Gravity Collaboration, Abuter, R., Amorim, A., et al. 2019, *Astronomy and Astrophysics*, 625, L10, doi: [10.1051/0004-6361/201935656](https://doi.org/10.1051/0004-6361/201935656)
- Guo, R., Li, Z.-Y., Shen, J., Mao, S., & Liu, C. 2024, *The Astrophysical Journal*, 960, 133, doi: [10.3847/1538-4357/ad037b](https://doi.org/10.3847/1538-4357/ad037b)
- Guo, R., Liu, C., Mao, S., et al. 2020, *Monthly Notices of the Royal Astronomical Society*, 495, 4828, doi: [10.1093/mnras/staa1483](https://doi.org/10.1093/mnras/staa1483)
- Guo, R., Shen, J., Li, Z.-Y., Liu, C., & Mao, S. 2022, *The Astrophysical Journal*, 936, 103, doi: [10.3847/1538-4357/ac86cd](https://doi.org/10.3847/1538-4357/ac86cd)
- Hao, C. J., Xu, Y., Hou, L. G., et al. 2021, *Astronomy and Astrophysics*, 652, A102, doi: [10.1051/0004-6361/202140608](https://doi.org/10.1051/0004-6361/202140608)
- Hattori, K., Valluri, M., & Vasiliev, E. 2021, *Monthly Notices of the Royal Astronomical Society*, 508, 5468, doi: [10.1093/mnras/stab2898](https://doi.org/10.1093/mnras/stab2898)
- Hellwing, W. A., Frenk, C. S., Cautun, M., et al. 2016, *Monthly Notices of the Royal Astronomical Society*, 457, 3492, doi: [10.1093/mnras/stw214](https://doi.org/10.1093/mnras/stw214)
- Hunt, J. A. S., & Kawata, D. 2013, *Monthly Notices of the Royal Astronomical Society*, 430, 1928, doi: [10.1093/mnras/stt021](https://doi.org/10.1093/mnras/stt021)
- Jeans, J. H. 1915, *Monthly Notices of the Royal Astronomical Society*, 76, 70, doi: [10.1093/mnras/76.2.70](https://doi.org/10.1093/mnras/76.2.70)
- Kaasalainen, M., & Binney, J. 1994, *Monthly Notices of the Royal Astronomical Society*, 268, 1033, doi: [10.1093/mnras/268.4.1033](https://doi.org/10.1093/mnras/268.4.1033)
- Kafle, P. R., Sharma, S., Lewis, G. F., & Bland-Hawthorn, J. 2014, *The Astrophysical Journal*, 794, 59, doi: [10.1088/0004-637X/794/1/59](https://doi.org/10.1088/0004-637X/794/1/59)
- Klypin, A., Yepes, G., Gottlöber, S., Prada, F., & Heß, S. 2016, *Monthly Notices of the Royal Astronomical Society*, 457, 4340, doi: [10.1093/mnras/stw248](https://doi.org/10.1093/mnras/stw248)
- Lim, S. H., Putney, E., Buckley, M. R., & Shih, D. 2025, *Journal of Cosmology and Astroparticle Physics*, 2025, 021, doi: [10.1088/1475-7516/2025/01/021](https://doi.org/10.1088/1475-7516/2025/01/021)
- Lin, H.-N., & Li, X. 2019, *Monthly Notices of the Royal Astronomical Society*, 487, 5679, doi: [10.1093/mnras/stz1698](https://doi.org/10.1093/mnras/stz1698)
- Lindgren, L., Bastian, U., Biermann, M., et al. 2021, *Astronomy and Astrophysics*, 649, A4, doi: [10.1051/0004-6361/202039653](https://doi.org/10.1051/0004-6361/202039653)
- Liu, C., Deng, L.-C., Carlin, J. L., et al. 2014, *The Astrophysical Journal*, 790, 110, doi: [10.1088/0004-637X/790/2/110](https://doi.org/10.1088/0004-637X/790/2/110)
- Long, R. J., Mao, S., Shen, J., & Wang, Y. 2013, *Monthly Notices of the Royal Astronomical Society*, 428, 3478, doi: [10.1093/mnras/sts285](https://doi.org/10.1093/mnras/sts285)
- Lovell, M. R., Pillepich, A., Genel, S., et al. 2018, *Monthly Notices of the Royal Astronomical Society*, 481, 1950, doi: [10.1093/mnras/sty2339](https://doi.org/10.1093/mnras/sty2339)
- Luri, X., Brown, A. G. A., Sarro, L. M., et al. 2018, *Astronomy and Astrophysics*, 616, A9, doi: [10.1051/0004-6361/201832964](https://doi.org/10.1051/0004-6361/201832964)
- Mackereth, J. T., Bovy, J., Leung, H. W., et al. 2019, *Monthly Notices of the Royal Astronomical Society*, 489, 176, doi: [10.1093/mnras/stz1521](https://doi.org/10.1093/mnras/stz1521)
- McGill, C., & Binney, J. 1990, *Monthly Notices of the Royal Astronomical Society*, 244, 634
- McMillan, P. J. 2017, *Monthly Notices of the Royal Astronomical Society*, 465, 76, doi: [10.1093/mnras/stw2759](https://doi.org/10.1093/mnras/stw2759)
- McMillan, P. J., & Binney, J. J. 2008, *Monthly Notices of the Royal Astronomical Society*, 390, 429, doi: [10.1111/j.1365-2966.2008.13767.x](https://doi.org/10.1111/j.1365-2966.2008.13767.x)

- McMillan, P. J., Petersson, J., Tepper-Garcia, T., et al. 2022, *Monthly Notices of the Royal Astronomical Society*, 516, 4988, doi: [10.1093/mnras/stac2571](https://doi.org/10.1093/mnras/stac2571)
- Monari, G., Famaey, B., Carrillo, I., et al. 2018, *Astronomy and Astrophysics*, 616, L9, doi: [10.1051/0004-6361/201833748](https://doi.org/10.1051/0004-6361/201833748)
- Moreno, E., Fernández-Trincado, J. G., Schuster, W. J., Pérez-Villegas, A., & Chaves-Velasquez, L. 2021, *Monthly Notices of the Royal Astronomical Society*, 506, 4687, doi: [10.1093/mnras/stab1908](https://doi.org/10.1093/mnras/stab1908)
- Navarro, J. F., Frenk, C. S., & White, S. D. M. 1997, *The Astrophysical Journal*, 490, 493, doi: [10.1086/304888](https://doi.org/10.1086/304888)
- Pang, X., Tang, S.-Y., Li, Y., et al. 2022, *The Astrophysical Journal*, 931, 156, doi: [10.3847/1538-4357/ac674e](https://doi.org/10.3847/1538-4357/ac674e)
- Piffl, T., Binney, J., McMillan, P. J., et al. 2014, *Monthly Notices of the Royal Astronomical Society*, 445, 3133, doi: [10.1093/mnras/stu1948](https://doi.org/10.1093/mnras/stu1948)
- Planck Collaboration, Ade, P. A. R., Aghanim, N., et al. 2014, *Astronomy and Astrophysics*, 571, A1, doi: [10.1051/0004-6361/201321529](https://doi.org/10.1051/0004-6361/201321529)
- Planck Collaboration, Aghanim, N., Akrami, Y., et al. 2020, *Astronomy and Astrophysics*, 641, A6, doi: [10.1051/0004-6361/201833910](https://doi.org/10.1051/0004-6361/201833910)
- Poggio, E., Drimmel, R., Cantat-Gaudin, T., et al. 2021, *Astronomy and Astrophysics*, 651, A104, doi: [10.1051/0004-6361/202140687](https://doi.org/10.1051/0004-6361/202140687)
- Portail, M., Wegg, C., Gerhard, O., & Ness, M. 2017, *Monthly Notices of the Royal Astronomical Society*, 470, 1233, doi: [10.1093/mnras/stx1293](https://doi.org/10.1093/mnras/stx1293)
- Posti, L., & Helmi, A. 2019, *Astronomy and Astrophysics*, 621, A56, doi: [10.1051/0004-6361/201833355](https://doi.org/10.1051/0004-6361/201833355)
- Price-Whelan, A. M. 2017, *The Journal of Open Source Software*, 2, 388, doi: [10.21105/joss.00388](https://doi.org/10.21105/joss.00388)
- Robin, A. C., Bienaymé, O., Salomon, J. B., et al. 2022, *Astronomy and Astrophysics*, 667, A98, doi: [10.1051/0004-6361/202243686](https://doi.org/10.1051/0004-6361/202243686)
- Sanders, J. L., & Binney, J. 2016, *Monthly Notices of the Royal Astronomical Society*, 457, 2107, doi: [10.1093/mnras/stw106](https://doi.org/10.1093/mnras/stw106)
- Sanders, J. L., & Das, P. 2018, *Monthly Notices of the Royal Astronomical Society*, 481, 4093, doi: [10.1093/mnras/sty2490](https://doi.org/10.1093/mnras/sty2490)
- Schaller, M., Frenk, C. S., Bower, R. G., et al. 2015, *Monthly Notices of the Royal Astronomical Society*, 451, 1247, doi: [10.1093/mnras/stv1067](https://doi.org/10.1093/mnras/stv1067)
- Schönrich, R., Binney, J., & Dehnen, W. 2010, *Monthly Notices of the Royal Astronomical Society*, 403, 1829, doi: [10.1111/j.1365-2966.2010.16253.x](https://doi.org/10.1111/j.1365-2966.2010.16253.x)
- Schwarzschild, M. 1979, *The Astrophysical Journal*, 232, 236, doi: [10.1086/157282](https://doi.org/10.1086/157282)
- . 1993, *The Astrophysical Journal*, 409, 563, doi: [10.1086/172687](https://doi.org/10.1086/172687)
- Sun, G., Wang, Y., Liu, C., et al. 2023, *Research in Astronomy and Astrophysics*, 23, 015013, doi: [10.1088/1674-4527/ac9e91](https://doi.org/10.1088/1674-4527/ac9e91)
- Sun, W., Huang, Y., Shen, H., et al. 2024, *The Astrophysical Journal*, 961, 141, doi: [10.3847/1538-4357/ad06ad](https://doi.org/10.3847/1538-4357/ad06ad)
- Syer, D., & Tremaine, S. 1996, *Monthly Notices of the Royal Astronomical Society*, 282, 223, doi: [10.1093/mnras/282.1.223](https://doi.org/10.1093/mnras/282.1.223)
- Tarricq, Y., Soubiran, C., Casamiquela, L., et al. 2021, *Astronomy and Astrophysics*, 647, A19, doi: [10.1051/0004-6361/202039388](https://doi.org/10.1051/0004-6361/202039388)
- Tian, H.-J., Liu, C., Carlin, J. L., et al. 2015, *The Astrophysical Journal*, 809, 145, doi: [10.1088/0004-637X/809/2/145](https://doi.org/10.1088/0004-637X/809/2/145)
- Valluri, M., & Merritt, D. 1999, in *Astronomical Society of the Pacific Conference Series*, Vol. 182, *Galaxy Dynamics - A Rutgers Symposium*, ed. D. R. Merritt, M. Valluri, & J. A. Sellwood, 178, doi: [10.48550/arXiv.astro-ph/9906176](https://doi.org/10.48550/arXiv.astro-ph/9906176)
- Vasiliev, E. 2018, *arXiv e-prints*, arXiv:1802.08255, doi: [10.48550/arXiv.1802.08255](https://doi.org/10.48550/arXiv.1802.08255)
- . 2019a, *Monthly Notices of the Royal Astronomical Society*, 482, 1525, doi: [10.1093/mnras/sty2672](https://doi.org/10.1093/mnras/sty2672)
- . 2019b, *Monthly Notices of the Royal Astronomical Society*, 484, 2832, doi: [10.1093/mnras/stz171](https://doi.org/10.1093/mnras/stz171)
- Vieira, K., Carraro, G., Korchagin, V., et al. 2022, *The Astrophysical Journal*, 932, 28, doi: [10.3847/1538-4357/ac6b9b](https://doi.org/10.3847/1538-4357/ac6b9b)
- Wang, H.-F., Chrobáková, Ž., López-Corredoira, M., & Sylos Labini, F. 2023, *The Astrophysical Journal*, 942, 12, doi: [10.3847/1538-4357/aca27c](https://doi.org/10.3847/1538-4357/aca27c)
- Wang, Q., Wang, Y., Liu, C., Mao, S., & Long, R. J. 2017, *Monthly Notices of the Royal Astronomical Society*, 470, 2949, doi: [10.1093/mnras/stx1382](https://doi.org/10.1093/mnras/stx1382)
- Wang, W., Han, J., Cautun, M., Li, Z., & Ishigaki, M. N. 2020, *Science China Physics, Mechanics, and Astronomy*, 63, 109801, doi: [10.1007/s11433-019-1541-6](https://doi.org/10.1007/s11433-019-1541-6)
- Wang, Y., Mao, S., Long, R. J., & Shen, J. 2013, *Monthly Notices of the Royal Astronomical Society*, 435, 3437, doi: [10.1093/mnras/stt1537](https://doi.org/10.1093/mnras/stt1537)
- Wang, Y., Zhao, H., Mao, S., & Rich, R. M. 2012, *Monthly Notices of the Royal Astronomical Society*, 427, 1429, doi: [10.1111/j.1365-2966.2012.22063.x](https://doi.org/10.1111/j.1365-2966.2012.22063.x)
- Watkins, L. L., Evans, N. W., & An, J. H. 2010, *Monthly Notices of the Royal Astronomical Society*, 406, 264, doi: [10.1111/j.1365-2966.2010.16708.x](https://doi.org/10.1111/j.1365-2966.2010.16708.x)
- Webb, J. J., Hunt, J. A. S., & Bovy, J. 2023, *Monthly Notices of the Royal Astronomical Society*, 521, 3898, doi: [10.1093/mnras/stad762](https://doi.org/10.1093/mnras/stad762)
- Wenger, M., Ochsenbein, F., Egret, D., et al. 2000, *A&AS*, 143, 9, doi: [10.1051/aas:2000332](https://doi.org/10.1051/aas:2000332)
- Xiang, M., Shi, J., Liu, X., et al. 2018, *The Astrophysical Journal Supplement Series*, 237, 33, doi: [10.3847/1538-4365/aad237](https://doi.org/10.3847/1538-4365/aad237)
- Xu, Y., Liu, C., Tian, H., et al. 2020, *The Astrophysical Journal*, 905, 6, doi: [10.3847/1538-4357/abc2cb](https://doi.org/10.3847/1538-4357/abc2cb)

Xue, X. X., Rix, H. W., Zhao, G., et al. 2008, The Astrophysical
Journal, 684, 1143, doi: [10.1086/589500](https://doi.org/10.1086/589500)

Zhao, H. 1996, Monthly Notices of the Royal Astronomical
Society, 283, 149, doi: [10.1093/mnras/283.1.149](https://doi.org/10.1093/mnras/283.1.149)

Zhu, L., Long, R. J., Mao, S., et al. 2014, The Astrophysical
Journal, 792, 59, doi: [10.1088/0004-637X/792/1/59](https://doi.org/10.1088/0004-637X/792/1/59)

APPENDIX

A. VELOCITY DISTRIBUTION

In this appendix, we show the rest velocity distributions for the regions we consider.

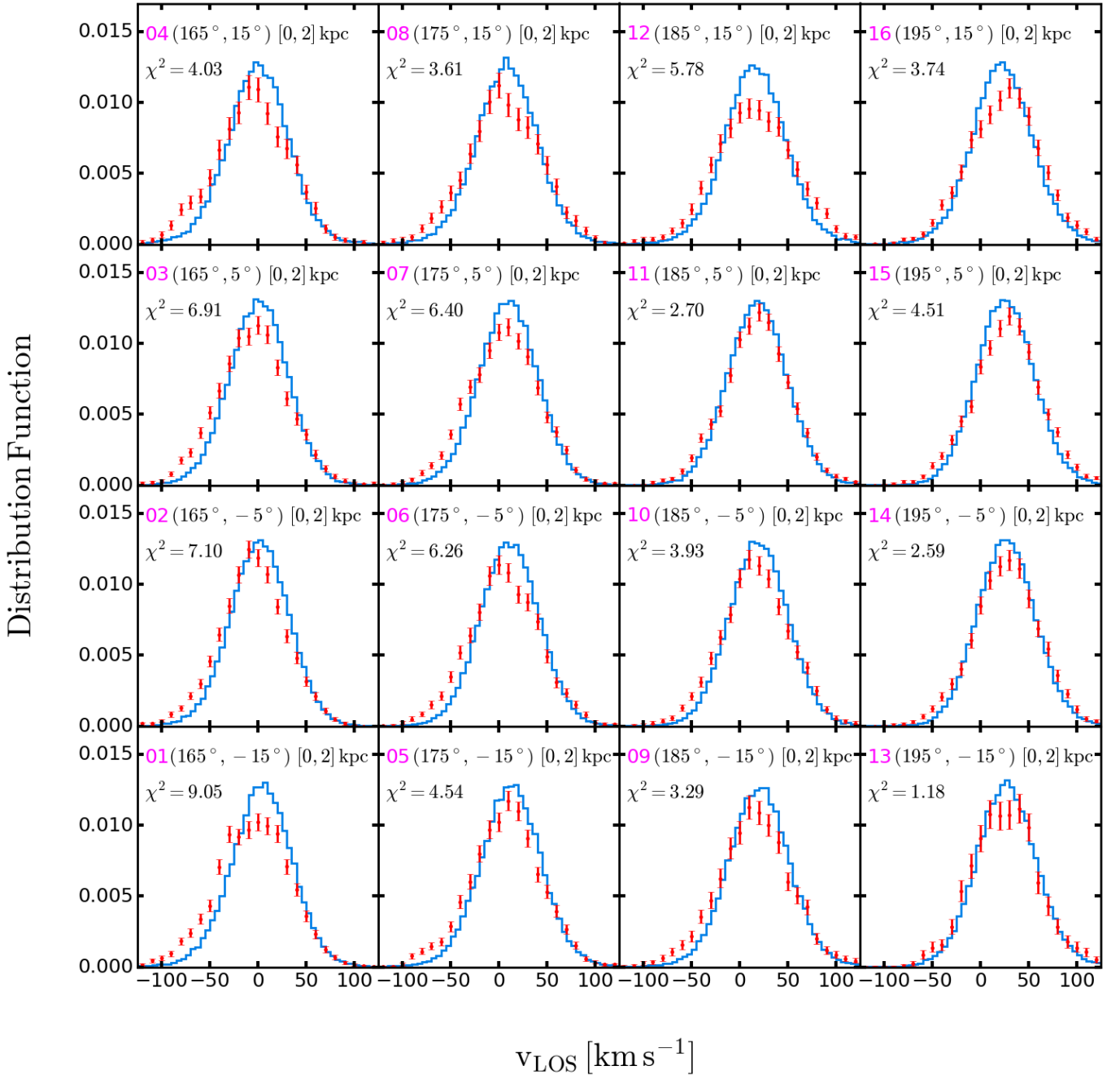


Figure A.1. The distribution function of the line-of-sight velocity (v_{LOS}) for sky regions 01-16, as defined in Table 1. Each sky region covers an area of $10^\circ \times 10^\circ$. The reduced χ^2 is indicated in each panel.

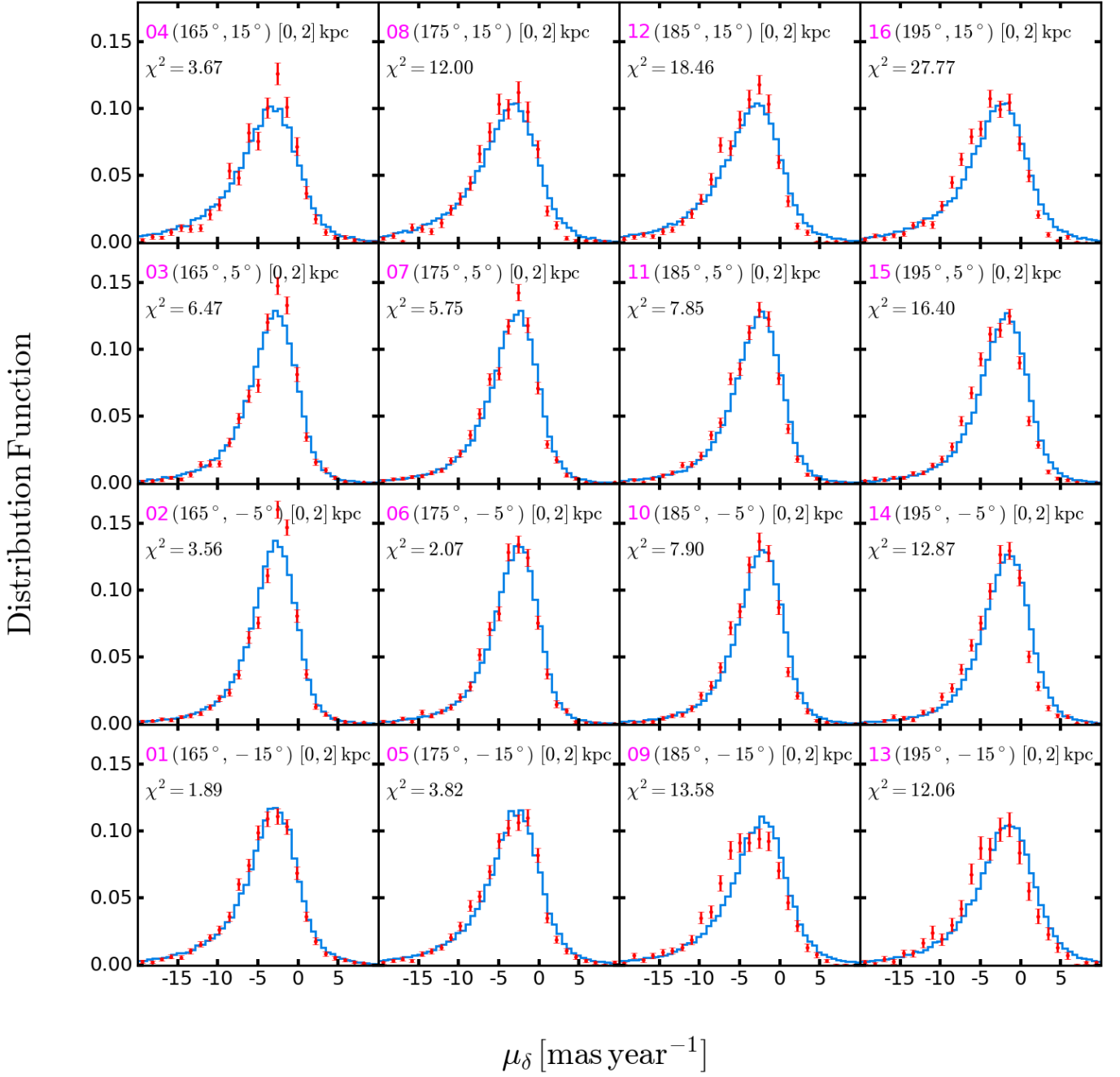


Figure A.2. The distribution function of proper motion in the declination direction (μ_δ) for sky regions 01-16, as defined in Table 1. Each sky region covers an area of $10^\circ \times 10^\circ$.

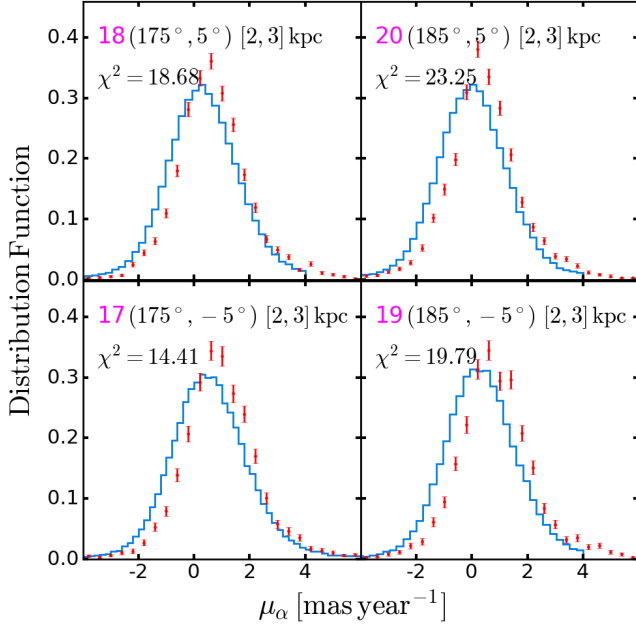


Figure A.3. The distribution function of proper motion along the right ascension (μ_α) for sky regions 17-20, as defined in Table 1. Each sky region covers an area of $10^\circ \times 10^\circ$.

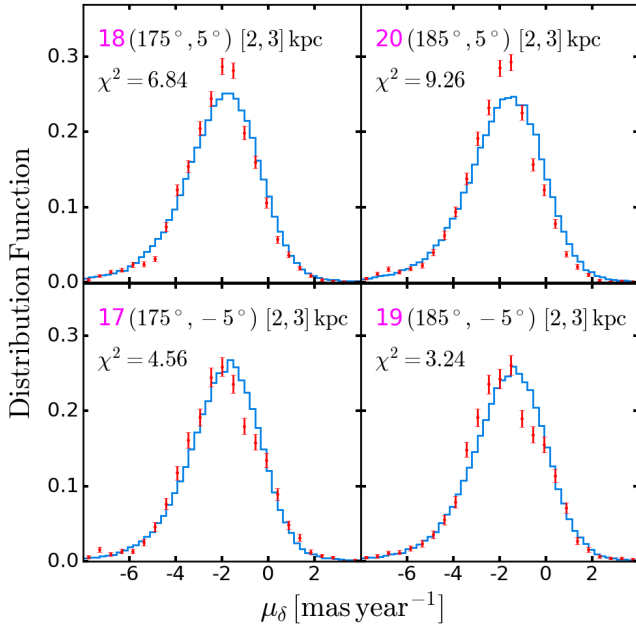


Figure A.4. The distribution function of proper motion in the declination direction (μ_δ) for sky regions 17-20, as defined in Table 1. Each sky region covers an area of $10^\circ \times 10^\circ$.

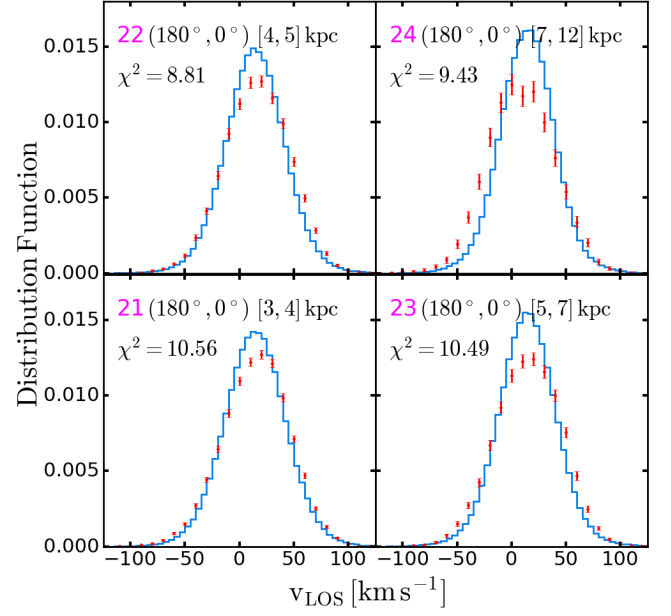


Figure A.5. The distribution function of the line-of-sight velocity (v_{LOS}) for sky regions 21-24, as defined in Table 1. Each sky region covers an area of $20^\circ \times 20^\circ$.

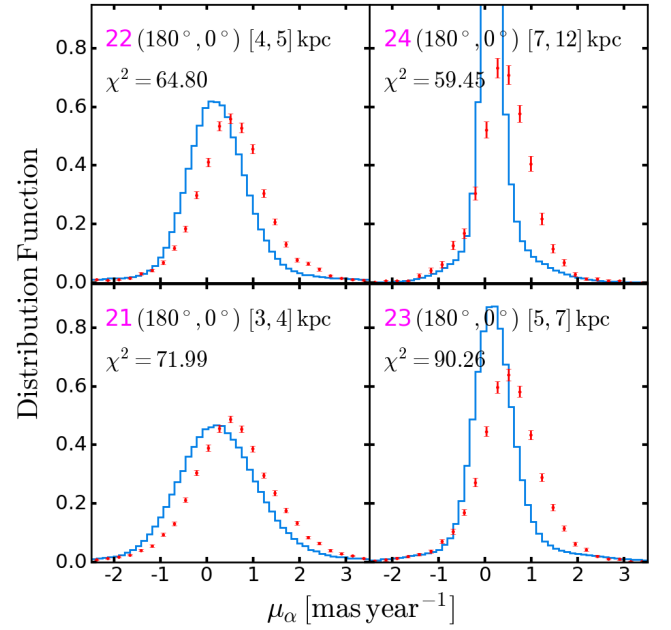


Figure A.6. The distribution function of proper motion along the right ascension (μ_α) for sky regions 21-24, as defined in Table 1. Each sky region covers an area of $20^\circ \times 20^\circ$.

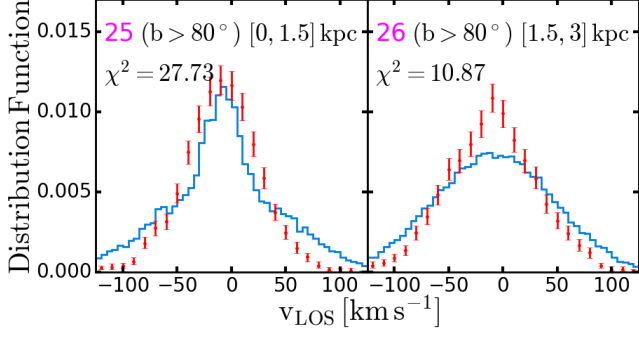


Figure A.7. The distribution function of the line-of-sight velocity (v_{LOS}) for sky regions 25 and 26, as defined in Table 1. Each sky region covers a circle with a diameter of 10° .

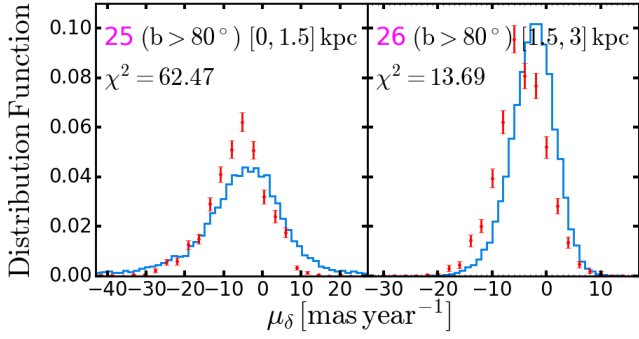


Figure A.8. The distribution function of proper motion in the declination direction (μ_δ) for sky regions 25 and 26, as defined in Table 1. Each sky region covers a circle with a diameter of 10° .

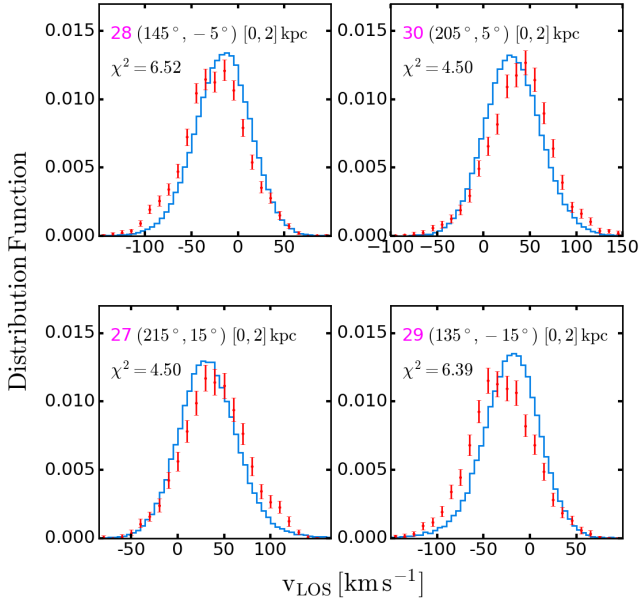


Figure A.9. The distribution function of the line-of-sight velocity (v_{LOS}) for sky regions 27-30, as defined in Table 1. Each sky region covers an area of $10^\circ \times 10^\circ$.

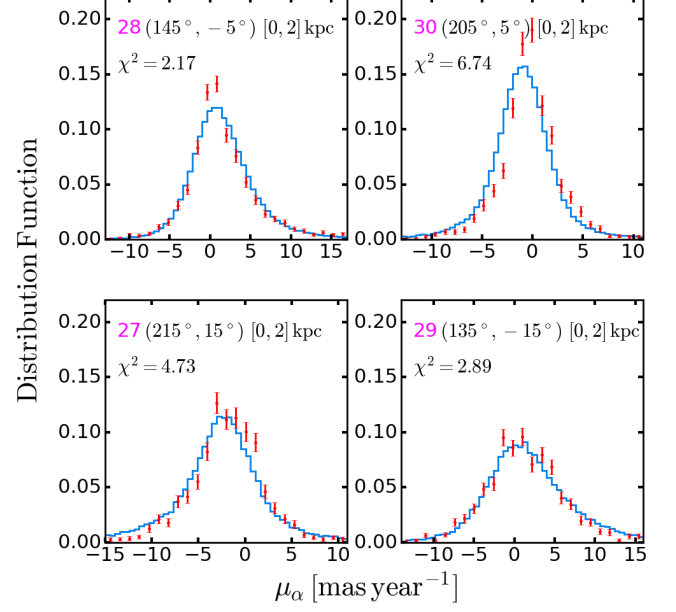


Figure A.10. The distribution function of proper motion along the right ascension (μ_α) for sky regions 27-30, as defined in Table 1. Each sky region covers an area of $10^\circ \times 10^\circ$.